minerals

MDPI

Article

Sandstone-Hosted Uranium Deposits as a Possible Source for Critical Elements: The Eureka Mine Case, Castell-Estaó, Catalonia

Montgarri Castillo-Oliver [1,*], Joan Carles Melgarejo [2], Lisard Torró [3], Cristina Villanova-de-Benavent [4], Marc Campeny [2,5], Yael Díaz-Acha [5], Sandra Amores-Casals [2], Jingyao Xu [6,7], Joaquin Proenza [2] and Esperança Tauler [2]

1 ARC Centre of Excellence for Core to Crust Fluid Systems (CCFS) and GEMOC, Department of Earth and Planetary Sciences, Macquarie University, North Ryde, NSW 2109, Australia
2 Departament de Mineralogia, Petrologia i Geologia Aplicada, Universitat de Barcelona, c/Martí i Franquès s/n, 08028 Barcelona, Spain; joan.carles.melgarejo.draper@ub.edu (J.C.M.); mcampenyc@bcn.cat (M.C.); sandra.amores.casals@gmail.com (S.A.-C.); japroenza@ub.edu (J.P.); esperancatauler@ub.edu (E.T.)
3 Geological Engineering Program, Faculty of Sciences and Engineering, Pontifical Catholic University of Peru (PUCP), Av. Universitaria 1801, San Miguel, Lima-32, Peru; lisardtorro@hotmail.com
4 School of Environment and Technology, Applied Geosciences Research and Enterprise Group, University of Brighton, Cockcroft Building, Lewes Road, Brighton BN4 2GJ, UK; c.villanova-de-benavent@brighton.ac.uk
5 Museu de Ciències Naturals de Barcelona, Parc de la Ciutadella s/n, 08003 Barcelona, Spain; ydiaz@bcn.cat
6 State Key Laboratory of Lithospheric Evolution, Institute of Geology and Geophysics, Chinese Academy of Sciences, Beijing 100029, China; moiraxjy@hotmail.com
7 Innovation Academy for Earth Science, Chinese Academy of Sciences, Beijing 100029, China
* Correspondence: montgarri.castillo-oliver@mq.edu.au

Received: 3 December 2019; Accepted: 24 December 2019; Published: 30 December 2019

Abstract: The Eureka deposit in Castell-estaó in the Catalan Pyrenees is a Cu–U–V deposit, hosted by Triassic red-bed sandstones, and classified here as a low-temperature, sandstone-hosted stratabound metamorphite U deposit. The main mineralisation is stratabound, related to coal-bearing units and produced during the Alpine deformation by migration of hydrothermal fluids. In this stage, the original sedimentary and diagenetic components (quartz and calcite, micas, hematite and locally apatite) were replaced by a complex sequence of roscoelite, fine-grained REE phosphates, sulphides and Ni–Co arsenides and sulpharsenides, Ag–Pb selenides, bismuth phases, sulphosalts and uraninite. The black shales of the Silurian sediments underlying the deposit and the nearby Carboniferous volcanoclastic rocks are interpreted as the source of the redox-sensitive elements concentrated in Eureka. The sulphur source is related to leaching of the evaporitic Keuper facies. The REE transport would be facilitated by SO_4-rich solutions. The reduction of these solutions by interaction with organic matter resulted in the widespread precipitation of REE and redox-sensitive elements, including many critical metals (V, Bi, Sb, Co), whereas barite precipitated in the oxidized domains. The occurrence of similar enrichments in critical elements can be expected in other similar large uranium deposits, which could be a source of these elements as by-products.

Keywords: critical metals; redox-sensitive elements; red bed; metamorphite; vanadium; uranium; copper; rare earth elements; cobalt; nickel; selenium

1. Introduction

The Eureka deposit has been historically classified as a sandstone-type uranium deposit hosted in a red-bed [1]. It was investigated in the 1960s as part of a development plan to find new resources

for nuclear power and weapons in Spain. The exploration operations included the digging of 4 tunnels at different depths, as well as two trenches near the Castell-estaó village (Catalonia). However, the mine was never productive and exploration was finally abandoned in the 1980s. Nowadays, the local government is starting a new project to re-open them as tourist mines. Despite the low economic value of the Eureka deposit, its extremely wide mineralogical diversity soon put it in the spotlight of the scientific community. Rare minerals (i.e., čejkaite, arsenuranylite, compreignacite, natrozippeite; [2]) have since then been described and the Eureka mine even became a type locality of new minerals (i.e., abellaite, [3]). However, its complete mineralogical assemblage and the processes that led to the formation of this deposit are still far from being fully constrained.Sandstone-type uranium deposits are defined as diagenetic concentrations of uranium minerals hosted in sandstone formations with a fluvial, lacustrine, or deltaic origin [4,5]. Although in the past these deposits were mainly mined for copper, within the 1940s, the Manhattan Project and the rapid increase of uranium mines in the Colorado Plateau playing out at the beginning of the nuclear power era, they became an important source of uranium [6–8] in the major role in the mineralogical characterisation of this type of deposit [9–11]. Major uranium sandstone hosted deposits are also being mined in Australia, China, and Kazakhstan [12,13]. Sandstone deposits represent ~35% of the uranium deposits and ~28% of the world uranium resources [14]. In these deposits, reducing agents in the sediments (i.e., sulphides, coal seams, hydrocarbons, or organic matter) trigger the precipitation of metals with high valence states, typically U^{6+} and V^{5+} [15]. In other uranium sandstone deposits, hydrocarbons or H_2S released from underlying oil or gas fields were interpreted as the reducing agents [16,17], although tectonic control plays a major role in these cases [18].

These changes in the Eh of the environment, often coupled with variations in pH and temperature, can also lead to precipitation of many other elements, known as Redox Sensitive Elements (RSE). These elements typically include a wide range of metals (i.e., Fe, Mo, As, V, Sb, Se, Ni, Co, Cu, and Cr). Many of these elements are considered strategic metals, now in an increasing demand to meet the needs of the low-carbon energy technologies (i.e., PV cells, wind turbines, electric vehicles), the modern technologies (i.e., laptops, smartphones, touch screens, etc.), and chemicals and fertilizers [19–21]. Recent studies have shown that the demand of most of these elements will by 2030 be at least 20 times higher than the current demand [22]. Additionally, critical elements are usually irreplaceable and still not easily recycled [21]. Finally, the reserves of many of these elements remain low and their market is controlled by a few countries [22]. Therefore, a better understanding of the genesis of the deposits concentrating these elements could provide to be key information to face the technological challenges of the coming decades.

In this manuscript, the mineralogical diversity of Eureka is regarded as an excellent opportunity to characterize the mechanisms of formation of critical elements-bearing minerals in a sandstone-hosted uranium deposit. Moreover, the access to all the mine tunnels and outcrops not only allowed good 3D sampling of the deposit, but also the study of the recent formation of critical-element-bearing minerals after remobilization of the primary mineral associations. A re-interpretation of the type of deposit towards a metamorphite-type is also proposed in this paper.

2. Geological Setting

2.1. Regional Geology

The Eureka mining complex is found in the central part of the Pyrenees, at the NW of the Pallars Jussà region in Catalonia, between Castell-estaó and the La Plana de Mont-Ros villages. Three main geological units can be distinguished in this domain: a pre-Hercynian Paleozoic basement, a post-Hercynian Paleozoic series and the Triassic rocks ([23]; Figure 1). The pre-Hercynian Paleozoic basement mainly consists of black shales of Silurian age, limestones of Devonian age and turbidites of the Lower Carboniferous, affected by folding and low-grade metamorphism during the Hercynian orogeny [23,24]. The Hercynian deformation in the Pyrenees has been linked to a transpressive regime,

characterized by low-P high-T metamorphism in the major domes. The main peak of metamorphism and syn-orogenic intrusions were dated at ~320–315 Ma [25], whereas late syn-orogenic to post-orogenic intrusions took place ~300 Ma [26,27].

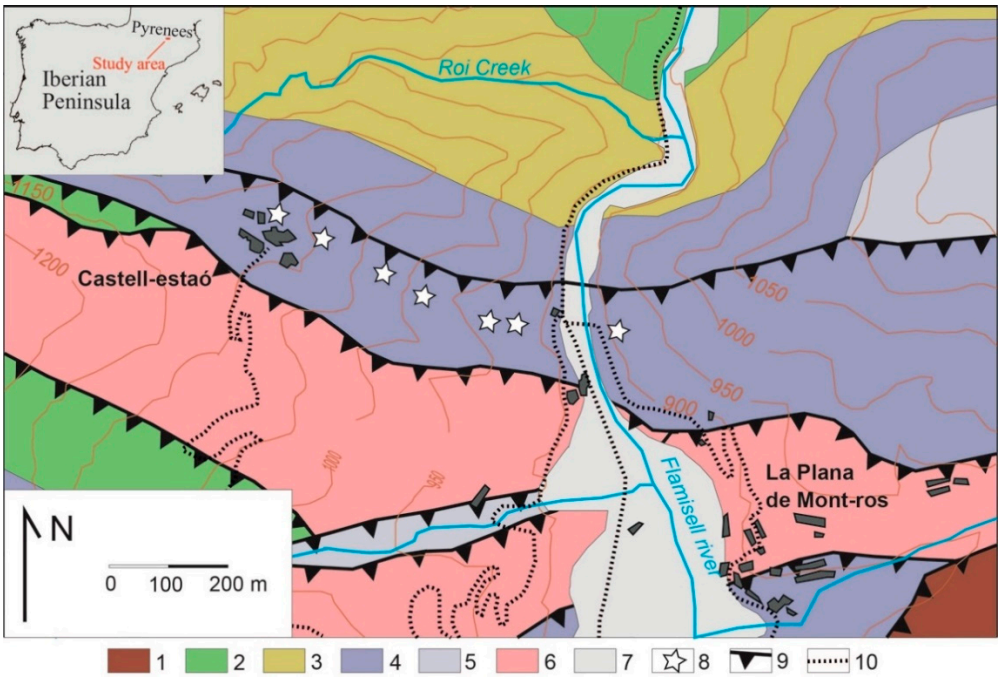

Figure 1. Geological map of the studied area. 1, Black shales (Silurian); 2, limestones (Devonian); 3, turbidites (Carboniferous); 4, sandstones, conglomerates, mudstones and coal (Buntsandstein facies, Lower Triassic); 5, limestones (Muschelkalk facies, Middle Triassic); 6, sandstones, gypsum, mudstones (Keuper facies, Upper Triassic); 7, alluvial sediments (Quaternary); 8, mining operations; 9, thrust; 10, road. Modified after the ICGC [28].

These layers are unconformably covered by a thick Upper-Carboniferous to Late Permian red-bed unit, which interbeds coal seams and calk-alkaline lavas and volcanoclastic rocks [29–33]. All these units are, in turn, unconformably covered by the Triassic series [34]. The Triassic series start with a thinning-upwards sequence of red quartz-rich conglomerates, sandstones, and mudstones in Buntsandstein facies (up to 290 m in thickness, with Olenekian-Anisian age; [35]). These series have been interpreted as alluvial-fan conglomerates, followed by sandy braided-river deposits [36–38]. The Bundsandtein facies is followed by ~80 m of subtidal-supratidal limestones of the Middle Triassic (in Muschelkalk facies; Ladinian-earliest Carnian after [34,39]) and a ~850 m thick sequence of reddish claystones and evaporites of the Upper Triassic in Keuper facies (Carnian-Norian; [40]).

Sills of tholeiitic diabase (locally known as ophites) are interbedded with the Keuper sedimentary rocks. The emplacement of these sills has been related to fracturing prior to the Atlantic opening [41], at the Triassic-Jurassic boundary. Scapolitisation of these rocks by interaction with sulphate-rich fluids equilibrated with the host evaporites has been observed [42].

The Jurassic series is represented by 500 to 1000 m-thick beds of limestones, dolostones, marly limestones, and marls, with local occurrence of evaporites. The overlying Lower Cretaceous series is characterized by variable thickness (100 m to 4 km) and significant lateral facies changes [43]. These changes have been mainly tectonically controlled by extensional faults in a rifting context from the Lower Cretaceous-middle Cenomanian [44]. The sedimentation of marls and limestones between the Albian and the Santonian has been interpreted as a post-rift stage. The occurrence of syntectonic turbiditic sediments in some Upper Cretaceous basins has been linked to the onset of the compressive events of the Alpine orogeny [45]. During these early compressional stages, the extensional faults were reactivated as thrusts [44]. In the Paleogene, the deformation evolved to form an ensemble of thrust

structures trending E–W [46–48] and resulted in antiformal thrust stacking [49]. During the Paleogene, syntectonic coarse detrital sediments were deposited in piggy-back basins.

A poorly developed slaty cleavage can be locally observed in the Triassic metasedimentary rocks. Very low-grade metamorphism, in prehnite-pumpellyite facies, has been reported in the Triassic rocks of the area [50].

2.2. Stratigraphy of the Eureka Deposit

The uranium deposits studied here are hosted by the Early Triassic red-bed clastic series in the Buntsandstein facies [1]. The red-bed units have variable thickness, ranging between a few tens of meters to some hundreds, and extend from E to W along the Pyrenees. The ores occur in greenish units enriched in organic matter, in part vegetal debris and bituminous impregnations (Figure 2).

Figure 2. Image of the main Eureka mine outcrops, with Castell-estaó village at the top of the Uixer hill. Note the Buntsandstein red sandstones that host the mineralisation, dipping approximately 60° to the South (to the left of the image). The grey outcrops at the right part of the image correspond to Paleozoic rocks. The main mine dumps can be seen half-way up the mountain.

The lower unit of the Triassic sequence is found in the Uixer Hill and is defined by sandstone levels, often thicker than 50 m, which dip about 60° to the South. Fifty meters of reddish mudstones, interbedded with some fine-grained sandstones, overthrust these rocks, and are followed by the 5 m-thick greyish-green clastic unit that hosts the Cu–V–U mineralisation (Figure 3). This unit is followed by more than 50 m of interbedded reddish sandstones and mudstones. The mineralisations have lensoidal shape and are more than 50 m in length, with a thickness of up to 2 m. Disseminated mineralisation is directly related to beds enriched in organic matter. Each sedimentary layer usually shows a fining-upward grain size and an erosive base, with planar lamination typically at the bottom of the layer and cross lamination and ripples on the top. Similar lenses occur along the SE; all of them were explored for U in the 1950s. Ores are fine-grained and occur as the cement of the coarse units or following the schistosity in the shale units.

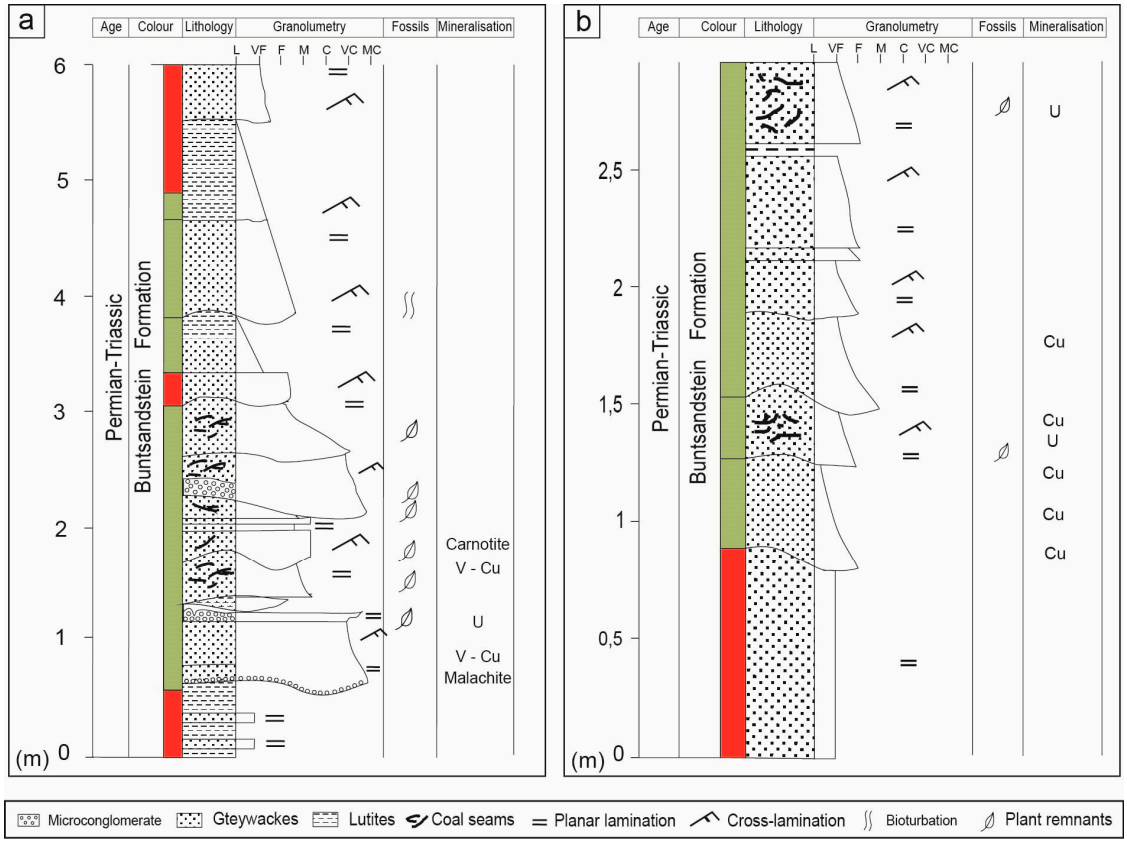

Figure 3. Stratigraphic profiles of the mineralized unit at the western outcrop at Castell-estaó (**a**) and at the easternmost outcrop (**b**). Note that the green-ish color of the sediments is commonly associated with the main coal seams, which contrasts with the red color characteristic of the red bed sandstones in the Eureka mine.

Mining in the Eureka deposit comprises several trenches on Cu–U outcrops and three tunnels at different levels connected by pits. These mines are arranged following the WNW–ESE trending bedding of the sandstones.

3. Materials and Methods

More than eighty samples were collected in the study area, which cover all stages of mineralisation at all levels of this red-bed deposit. Fifty polished thin sections and thirty polished mounts were prepared at the thin section laboratory of the Faculty of Geology at the University of Barcelona, Barcelona, Spain. After initial characterisation of the mineralisation using a petrographic microscope, the most representative thin sections and mounts were C-coated to be studied in detail by means of two SEM instruments from the CCiT-UB laboratories (Universitat de Barcelona, Barcelona, Spain): a SEM Leica Cambridge S.360 and an ESEM Quanta 200 FEI XTE 325/D8395 electron microscope with an INCA Energy 250 EDS detector attached. A focused beam of 25–30 keV was used in order to excite the weakest lines (K, L) of some heavy elements that could have some spectral interferences (U–K, Pb–Bi–Mo–S, Pb–As, etc.), at 1 nA and at a working distance of 10 mm. Chemical compositions of minerals were analyzed at the same facilities by means of a CAMECA SX50 electron microprobe, with four wavelength dispersive spectrometers (WDS). Analytical conditions were 20 keV accelerating potential, a beam current of 10 nA and a take off angle of 40°. For major and minor elements, counting times were 10 s for the peak and 10s for the background. Standards used for calibration for sulphides, arsenides, and sulphosalts were: pyrite (S, PET, Kα), pyrite (Fe, LIF, Kα), metallic Co (Co, LIF, Kα), NiO (Ni, LIF, Kα), chalcopyrite (Cu, LIF, Kα; S, PET, Kα), GaAs (As, TAP, Lβ), InSb (Sb, LIF, Lα), sphalerite (Zn, LIF, Kα), Bi_2Se (Se, LIF, Kα), Ag_2S (Ag, PET, Lα), galena (Pb, PET, Mα) and Bi_2Se (Bi, PET, Mα);

for oxidized minerals: albite (Na, TAP, Kα), apatite (P, PET, Kα), chalcopyrite (S, PET, Kα), orthoclase (K, PET, Kα), wollastonite (Ca, PET, Kα), metallic V (V, LIF, Kα), pyrite (Fe, LIF, Kα), chalcopyrite (Cu, LIF, Kα), GaAs (As, TAP, L β), Bi_2Se (Se, LIF, Lα), galena (Pb, PET, Mα), uraninite (U, PET, Mα), periclase (Mg, TAP, Kα), Al_2O_3 (Al, TAP, Kα), diopside (Si, TAP, Kα), hematite (Fe, LIF, Kα), barite (Ba, LIF, Lα), uraninite (U, PET, Mα). Some minerals were identified by means of X-ray powder diffraction (XRD). The XRD equipment was a PANalytical XPert PRO MPD alpha1 diffractometer located at the CCiT-UB (Barcelona, Spain), with a focalizer primary monochromator and an Xcelerator detector. The radiation used was Ko1 Cu (λ = 1.5406 Å) at 45 kV and 40mA. Spectra were interpreted using the software PANalytical XPert JCPDS.

4. Mineralisation Styles

Three different styles of mineralisation have been identified in the Eureka mine complex: stratabound mineralisation, vein mineralisation, and supergene mineralisation.

4.1. Stratabound Mineralisation

The main Cu–U–V mineralisation of the Eureka mine complex is found in the 5 m-thick greyish-green clastic unit embedded between the two thick (~50 m) layers of sandstones and mudstones that form the lower Triassic red bed sequence (Figure 4a). This grey unit comprises conglomerates and coarse sandstones, interlayered with very fine-grained sandstones and shales, which contain thin coal seams (Figures 3 and 4b,c). The stratabound mineralisation occurs as lenses directly related to these organic matter-rich levels, is up to 2 m thick and can be followed for more than 50 m along strike. Most of the minerals formed at this stage are fine-grained and occur either as the cement of the coarse-grained units or following the schistosity in the shale units.

4.2. Vein Mineralisation

Small veinlets, up to 1 cm in width, occur in the Castell-estaó outcrop, filling open joints in the necking domains of the boudins developed in the most competent layers (i.e., coarse sandstones; Figure 4d). Veins related to these necking zones are filled with drusy ankerite and lesser amounts of barite and dolomite, with disseminated Cu sulphides (i.e., chalcocite, chalcopyrite, covellite and bornite). In the lower mines, very thin (<0.5 cm wide) veinlets with similar mineral assemblage occur. As shown in Figure 4e, some of these veinlets inside the mine tunnels have a lateral displacement of some centimeters through stratigraphic planes. Therefore, these mineralized veinlets are previous to or synchronous with the Alpine deformation, as they are cut and moved by layer-to-layer slide (Figure 4e). This type of sliding could be related to back-thrusting or to flexural slip folds [51]. In any case, these structures are clearly related to Alpine thrusting.

4.3. Supergene Mineralisation

Supergene mineralisation is prominent in the Castell-estaó outcrop, and it consists of a very complex Cu–U–V–Ni–Co–As association of oxidized minerals, which occur either as very thin crusts (<100 μm) or as efflorescences. These secondary minerals are formed by alteration of the stratabound mineralized layers, and to a lesser extent of the veinlets. In fact, although supergene mineralisation is mostly found directly on the primary mineralisation, it can impregnate zones far from it as well. Even if supergene mineralisation is not very significant in terms of volume, it is very visible due to its greenish and yellowish color. This mineralisation has also been observed on the walls of the mine tunnels, providing unequivocal evidence of a very recent formation (Figure 4f). Chrysocolla [$(Cu,Al)_2H_2Si_2O_5(OH)_4 \cdot nH_2O$] and calcite stalactites precipitated in some tunnels where the fluid circulation is more prominent.

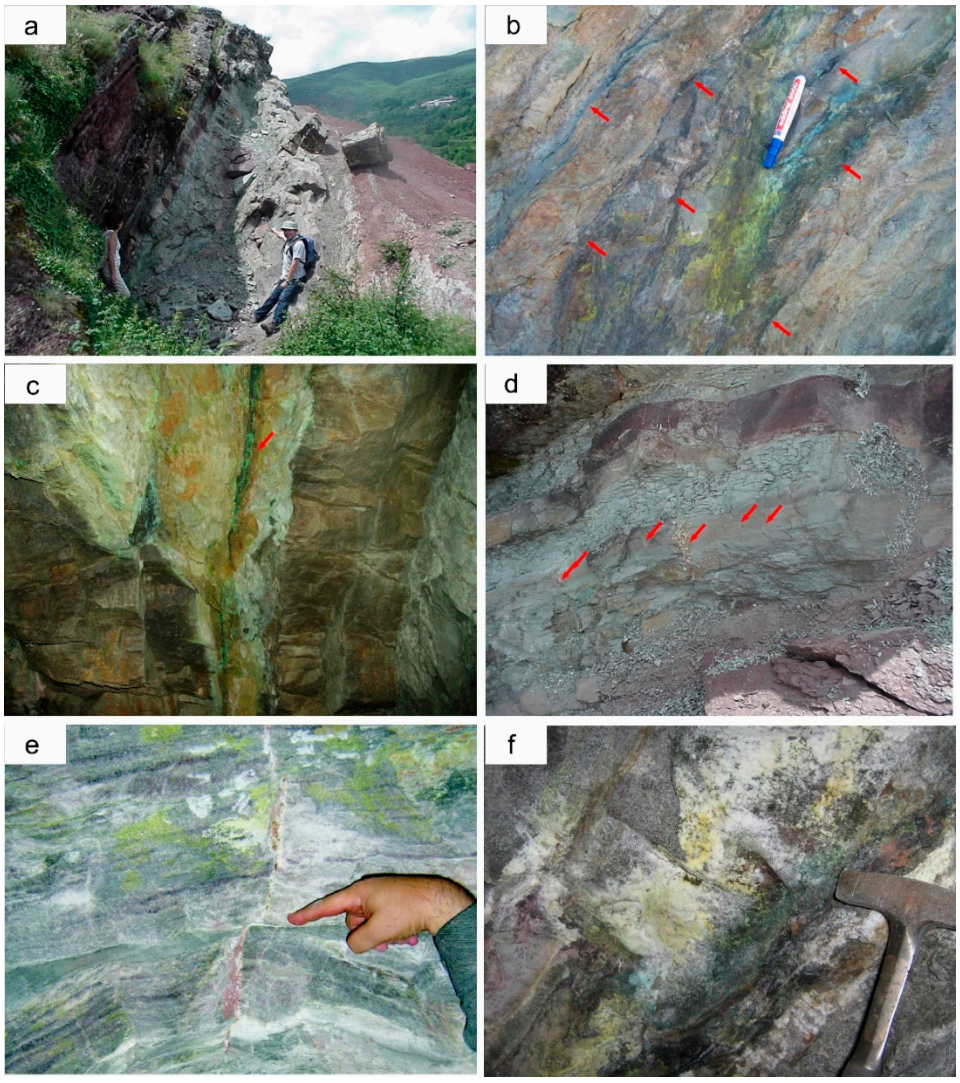

Figure 4. Field pictures showing the different mineralisation styles. (**a**) View of the upper outcrop (EUA), near Castell-estaó. Note the greenish sandstones sandwiched between the red units of sandstones (left) and shales (right); (**b**) Detail of the coal-rich units interbedded with sandstones; the yellow efflorescences are supergene uranyl vanadates, mainly carnotite; (**c**) Image of the coal seams in the lower mine (EUD), associated with copper enrichment (green crusts are brochantite); (**d**) Quartz-ankerite veins in necking domains (red arrows) in boudinaged sandstones embedded in shales; (**e**) Small veinlets displaced by layer-to-layer sliding; (**f**) Efflorescences of secondary uranium carbonates at the top of the middle tunnel (EUB).

5. Mineralogy and Textures

The textural and compositional characterisation of samples from the Eureka revealed a complex mineral sequence, with several episodes of overprinting of previous assemblages. To address the complexity of the processes involved in the formation of this deposit, the mineralogy of each stage is described separately below. The major element composition of the main minerals forming the diagenetic, stratabound and supergene stages have been included in the Supplementary Table S1.

5.1. Clastic Minerals from the Original Sediments

The host rocks have been studied to characterize the mineral associations existing prior to ore formation. They are mostly sandstones and polymictic quartz-rich conglomerates. These conglomerates are clast supported, dominated by quartz clasts and with variable amounts of rock clasts (mainly cherts

and metapelites, with low roundness). Even if the matrix content varies across the outcrop, the host rocks are here classified as litharenites of variable grain size. Table 1 summarizes the main mineralogy of the host rocks obtained from petrographic characterisation, including modal abundance, grain size and the most relevant textural features of each mineral.

Table 1. Composition of detrital particles in the sandstones of the Eureka deposit.

Mineral	Abundance (modal %)	Grain Size	Roundness, Texture, Habit	Other Features
Quartz	50–70	0.1–2 mm (mostly 1 mm)	usually rounded-subrounded (some angular)	Some show undulose extinction
K-feldspar and plagioclase	<5	0.1–2 mm (mostly 1 mm)	angular	variable degree of alteration
Biotite and muscovite	<0.5	<2 mm	tabular	Biotite often replaced by chlorite
Clays (illite)	1-10	very fine	forming planar aggregates	most likely illites (or smectites?)
Zircon	<1	50–100 μm	rounded	no metamictic or zoning
Tourmaline	<0.5	<100 μm	variable roundness	greenish-colour (schorl?)
Rutile	<0.5	<30 μm	rounded	strongly replaced
Rock fragments	15–30	Mostly 1–2 mm	low	Chert, intraclasts, metapelites

5.2. Diagenetic Stage

Early diagenesis led to compaction of sediments, resulting in the formation of sutured boundaries among quartz grains and the precipitation of syntaxial quartz cement (Figure 5a). The transformation of plant remnants to coal took also place in this early stage of diagenesis.

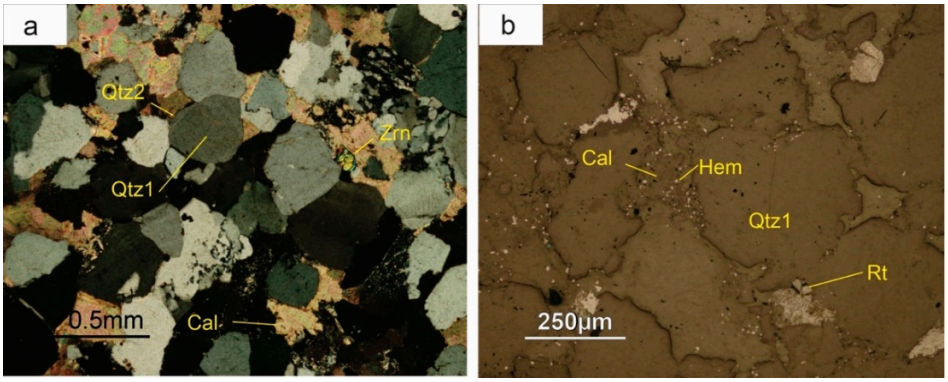

Figure 5. Microphotographs of the cements in the red beds. (**a**) Cement sequence in the red beds: dirty detrital quartz (Qtz1) with clean rims of syntaxial quartz cement (Qtz2), followed by sparry calcite cement (Cal). Note a detrital zircon grain (Zrn). Transmitted light, cross-polarized light (XPL); (**b**) Detrital quartz grains in the red beds (Qtz1) cemented by hematite (Hem) and calcite (Cal). Small rutile grains (Rt) are also found in the host rocks. Reflected light, plane-polarized light (PPL). All minerals in this manuscript follow the mineral abbreviation as suggested by IUGS [52].

The cement sequence continues with hematite, which gives the characteristic reddish colour to the red beds. It is a late cement and typically occurs as micrometric crystals, although it has also been observed as thin rims coating early quartz (Figure 5b). Sparry calcite usually fills the remaining porosity (Figure 5b), in some cases together with minor amounts of barite. Anatase occurs as scarce small (5–30 μm) euhedral crystals, with a characteristic bipyramidal habit. It predominantly concentrates near the boundaries of the detrital grains and is often corroded by sulphides. Millimeter-sized crystals of authigenic muscovite were also observed.

5.3. Stratabound Mineralisation

Stratabound mineralisation replaces the cements of the host rock. The original carbonate is replaced by early euhedral saddle crystals of dolomite-ankerite (Figure 6a), as well as a new generation of quartz. This quartz is either intergrown with carbonate or forms euhedral crystals. While the original calcite cement may still be present in the layers with low ore content (Figure 6b), it is completely absent in the more mineralized beds (Figure 6c). In these beds, the hematite cement has been totally replaced by a complex sulphide sequence. One of the most striking features of this event is the replacement of the clays in the matrix by roscoelite or V-rich micas, along with Ti–V oxides (schreyerite) and REE minerals (Figure 6c–e), along with a complex sequence of carbonates, quartz, apatite, arsenides, sulpharsenides, sulphides, sulphosalts, selenides, and uranium minerals.

An early generation of apatite has also been identified in many samples (Figure 6f). It typically occurs as hexagonal euhedral crystals (approximately of 0.1 mm in size), with a short prismatic habit and a bipyramidal terminations. Qualitative analyses by SEM show that all apatite crystals incorporate F in their structure, so we suggest that it is fluorapatite.

5.3.1. Roscoelite [$(K(V^{3+},Al,Mg)_2(AlSi_3O_{10})(OH)_2)$]

This mica is very common in the stratabound ores, in particular in the shales. It occurs as subhedral tabular crystals, ranging between 50 μm to 2mm in length. This mineral largely replaces the original detrital sheet silicates at the matrix, involving replacement of detrital quartz (Figure 6c), detrital micas or early diagenetic muscovite (Figure 6d). As it is one of the first minerals that form in this second stage, roscoelite is usually replaced by Cu sulphides, Ni–Co-sulphoarsenides and uranium minerals. In the highly-weathered domains it is replaced by a complex generation of vanadates.

5.3.2. V-rich Muscovite [$(K(Al,V^{3+})_2(AlSi_3O_{10})(OH)_2)$]

As described in the case of the large muscovite crystals, the fine-grained "illite" found in the groundmass of litharenite and shales is strongly replaced by fine-grained V-rich muscovite along grain contacts and cleavage (Figure 6d).

5.3.3. REE Minerals

REE minerals are very abundant in this locality and occur as fine-grained crystals (<5 μm), generally scattered within vanadian micas, mostly along cleavage. This suggests a late formation relative to micas (Figure 6d–f). Xenotime-(Y) [$(Y,HREE)PO_4)$] is very common in some sectors of the deposits, while monazite-(Ce) [$(Ce,LREE)PO_4)$] is less common. In addition, a fine-grained fibrous mineral having a composition that could fit in a REE-bearing crandallite [$(Ca,REE)Al_3(PO_4)(PO_3OH)(OH)_6$] is quite frequent in some places, although this mineral could be also formed during supergene episodes.

5.3.4. Schreyerite [$(V^{3+}{}_2Ti_3O_9)$]

This oxide mineral is scarce in the deposit and occurs as anhedral grains (<20 μm) associated with roscoelite (Figure 6f). It could also be produced by the replacement of clastic or authigenic Ti-bearing minerals. Schreyerite from the Eureka mine does not contain Cr or Sc, in contrast with other occurrences of this mineral in metamorphic deposits in Fennoscandia [53].

5.3.5. Bornite [(Cu_5FeS_4)] and Chalcopyrite [$(FeCuS_2)$]

The deposit is variably enriched in bornite and chalcopyrite. They usually replace calcite cement, especially at the boundaries of the mineralized bodies. Bornite grains are always anhedral, less than 200 μm in diameter, with very irregular boundaries and very often fractured. Bornite can replace chalcopyrite, resulting in a lamellar-textured pattern that resembles exsolutions (Figure 7a). These chalcopyrite lamellae are often either connected with the rims of the bornite grains or occur in the vicinity of cracks. Chalcopyrite and bornite can also occur as millimeter-scale anhedral crystals, not

related to these lamellae. Microprobe analysis yields almost stoichiometric compositions for bornite and chalcopyrite.

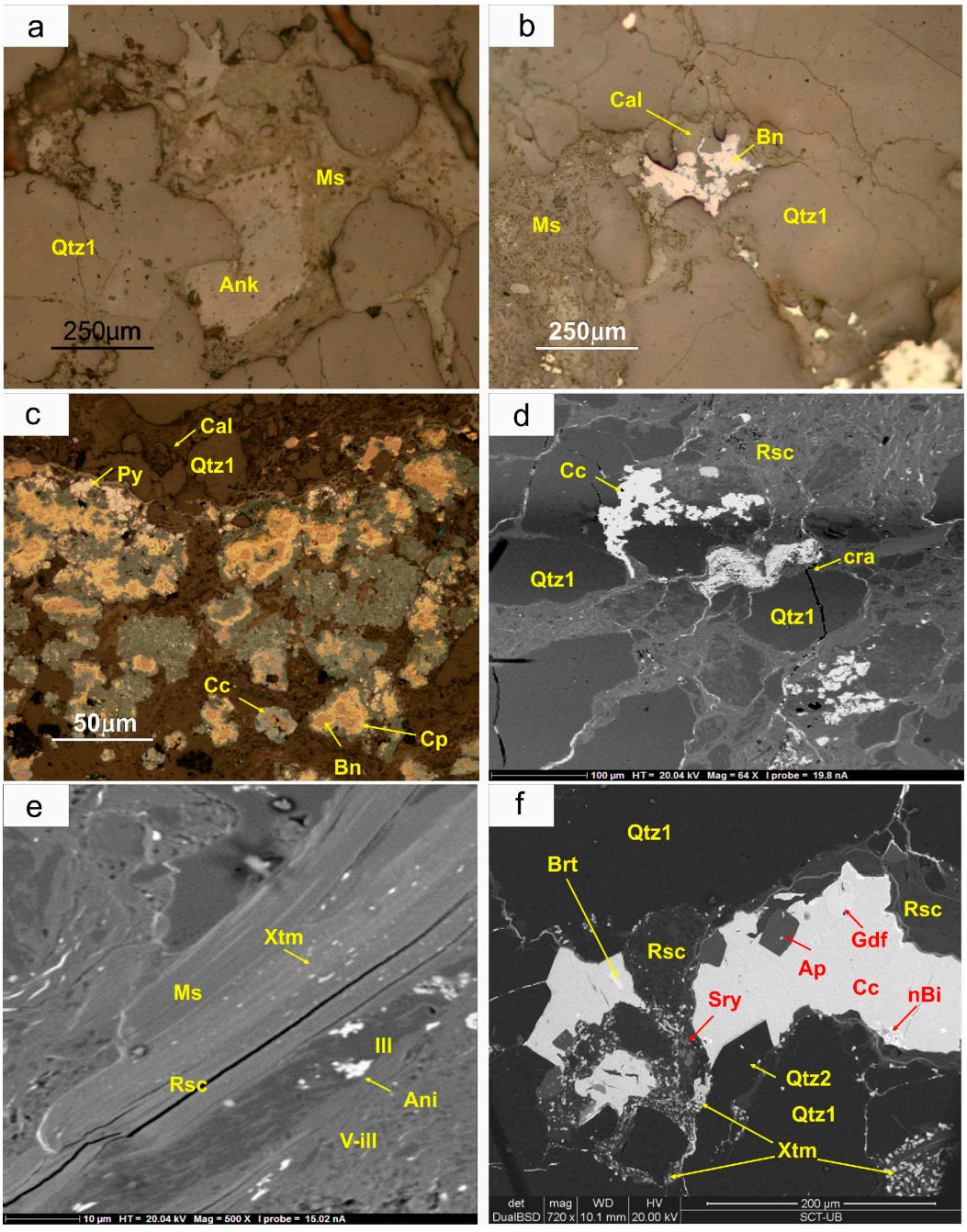

Figure 6. (**a**) Development of ankerite (Ank) rhombohedral crystals by replacement of the groundmass, with muscovite (Ms) and quart (Qtz1); note some small quartz crystals intergrown with ankerite (Ank) in the last bands; (**b**) Replacement of calcite cement (Cal) between detrital quartz (Qtz1) by bornite (Bn); (**c**) Advanced replacement of calcite cement and detrital grains by ores: pyrite (Py), bornite (Bn) mantled by chalcopyrite (Cp) and chalcocite (Cc); (**d**) Detrital quartz (Qtz1) in a roscoelite groundmass (Rsc) with chalcocite (Cc) and crandallite (Cra) scattered grains or filling slaty cleavage; (**e**) "illite" (Ill) and muscovite (Ms) plates replaced by "vanadian illite" (V-Ill) and roscoelite (Rsc), associated with xenotime (Xtm) and anilite (Ani); (**f**) Detrital quartz (Qtz1) overgrown by euhedral quartz (Qtz2) and apatite (Ap); clayish groundmass is replaced by roscoelite (Rsc) and large amounts of xenotime (Xtm), with minor schreyerite (Sry). Note the replacement of gersdorffite (Gdf) by chalcocite (Cc), native bismuth (nBi) and barite (Brt). (a) to (c), reflected light images, PPL; (d) to (f), SEM images, mode BSE.

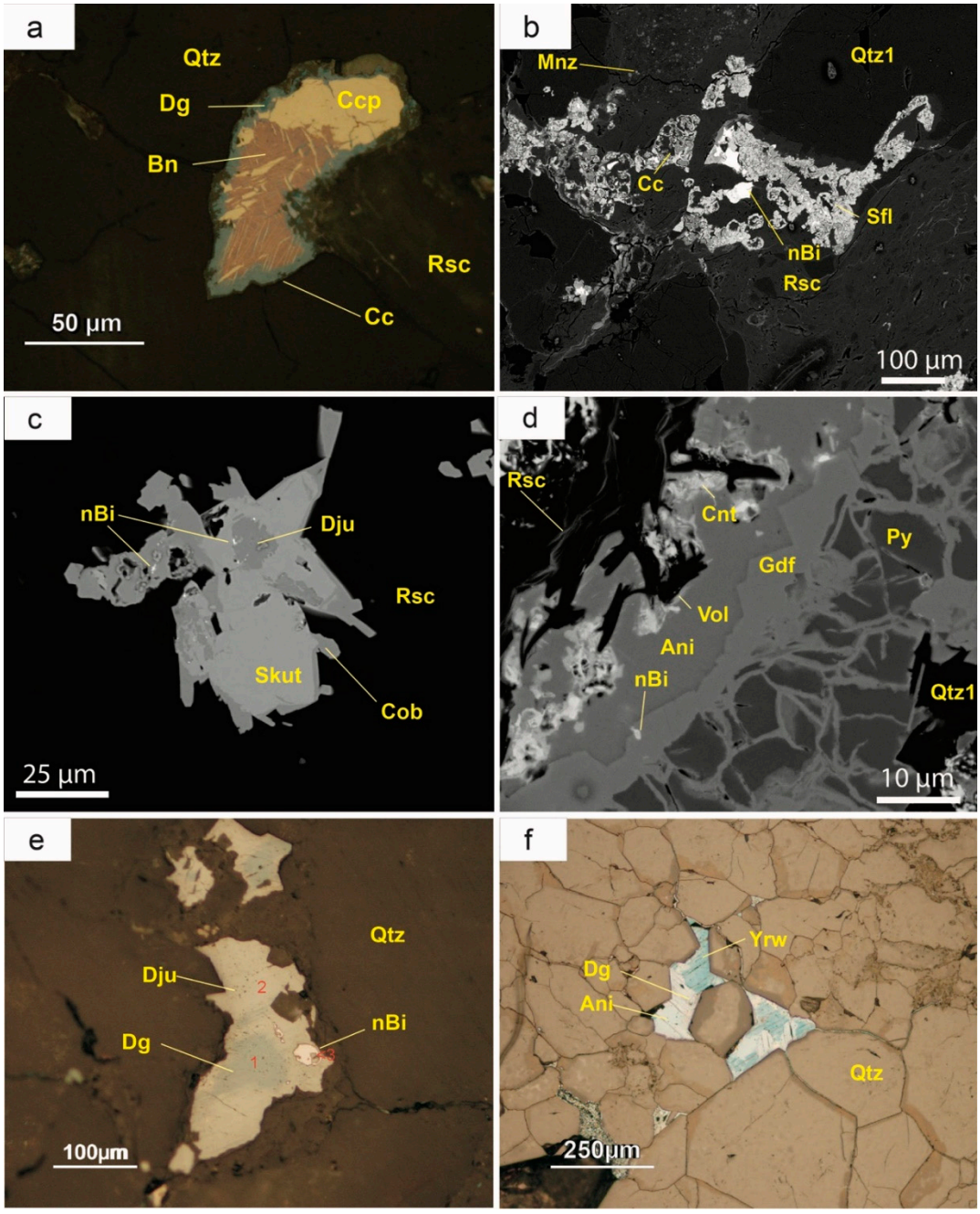

Figure 7. (**a**) Chalcopyrite grain (Ccp) interstitial to roscoelite (Rsc) and detrital quartz (Qtz), replaced by bornite (Bn), which was subsequently replaced by chalcopyrite (Cp) and finally by digenite (Dg) and chalcocite (Cc); (**b**) Chalcocite grains (Cc) interstitial to roscoelite (Rsc) with monazite (Mnz) and detrital quartz (Qtz1), mantled by safflorite (Sfl) and native bismuth (nBi); (**c**) Skutterudite grains (Skut), scattered in quartz (Qtz), mantling djurleite (Dju) and native bismuth (nBi). Skutterudite is mantled by cobaltite (Cob); (**d**) Pyrite (Py) was veined and overgrown by gersdorffite (Gdf) and native bismuth (nBi), and late anilite (Ani). Note quartz (Qtz) and roscoelite laths (Rsc) in the groundmass, partly replaced by carnotite (Cnt) and volborthite (Vol); (**e**) Digenite (Dg) replaced by djurleite (Dju) associated with native bismuth (nBi), interstitial to quartz (Qtz); (**f**) Digenite (Dg) interstitial to detrital quartz (Qtz), replaced by anilite (Ani) and finally by yarrowite (Yrw). (a,e,f) are reflected light images, PPL. (b–d) are SEM images, BSE mode.

5.3.6. Ni–Co Arsenides and Sulpharsenides

Ni–Co arsenides and sulpharsenides are among the most common ores in this deposit and occur as micrometric subhedral grains that either mantle copper minerals (Figure 7b), are scattered in the silicified groundmass (Figure 7c) or replace pyrite through cracks (Figure 7d). Ni–Co arsenides of the skutterudite-nickelskutterudite series (respectively $CoAs_3$ and $NiAs_3$) are found as euhedral or subhedral crystals with a dodecahedral habit, although skeletal forms are also present (Figure 7c). Safflorite ($CoAs_2$) is very common as subhedral rhombic crystals of 10–30 μm in diameter. In some cases, they mantle skutterudite or copper sulphides (Figure 7b). These arsenides, along with pyrite, are replaced by minerals of the cobaltite-gersdorffite series (Figure 7d). Gersdorffite-cobaltite crystals may be euhedral with octahedral forms {111}, generally less than 50 μm in diameter, but cobaltite mostly replaced skutterudite (Figure 7c). Microprobe analyses of arsenides and sulpharsenides show a wide range in Ni and Co contents, even within the same sample, ranging from end members to intermediate compositions between gersdorffite (NiAsS) and cobaltite (CoAsS). Undulose zoning was observed in these crystals and, in some cases, even a non-equilibrium crystallization, with corrosion of the previous grains. However, they are poor in Fe (less than 5 wt %), and Sb and PGE are below the detection limits of the electron microprobe.

5.3.7. Pyrite [FeS_2]

Pyrite was one of the first ore minerals to crystallize. It usually occurs as euhedral crystals tens of microns in diameter, concentrated as larger (sometimes centimetric) nests. These nests can be related to dark seams rich in organic matter. However, pyrite is typically fractured and partially or totally replaced by other ore minerals, mainly gersdorffite and Cu sulphides (Figure 7d).

5.3.8. Selenides

Isolated anhedral crystals of selenides some tens of microns in diameter are commonplace in the deposit. Naumannite (Ag_2Se) occurs as micrometric anhedral grains (Figure 8a). Its identification has been done by SEM, but its small grain size precludes the quantitative chemical analysis. Clausthalite (PbSe) is more abundant than galena in this deposit. Clausthalite occurs as veins associated with tennantite ($Cu_{12}As_4S_{13}$) or replacing covellite (CuS) and other Cu sulphides (Figure 8b). Clausthalite may be slightly enriched in silver (up to 0.41 wt %).

5.3.9. Minerals of the Chalcocite Group

Digenite (Cu_9S_5) is the most abundant Cu sulphide in this deposit. It occurs as subhedral, equant crystals and its diameter varies from 10 to 500 μm. It replaces carbonate grains and constitutes the main sulphide cement of the mineralized zone. Digenite usually shows a lamellar polysynthetic twinning, through which it is usually replaced by other Cu sulphides (djurleite, anilite, spionkopite, yarrowite, and covellite). However, these sulphides do not occur together. Finally, late formation of a fine-grained chalcocite (Cu_2S), usually as a replacement product of the abovementioned Cu sulphides, took place in some samples. Microprobe analysis of most minerals of this group yielded a low but significant proportion of Se (up to 0.43 wt %).

5.3.10. Covellite [CuS]

It is present in many samples as subhedral crystals from 20 to 100 μm in diameter, which partially or totally replace digenite grains. Covellite is commonly replaced by sulphosalts from the tetrahedrite-tennantite series. Covellite may concentrate up to 2.83 wt % Se.

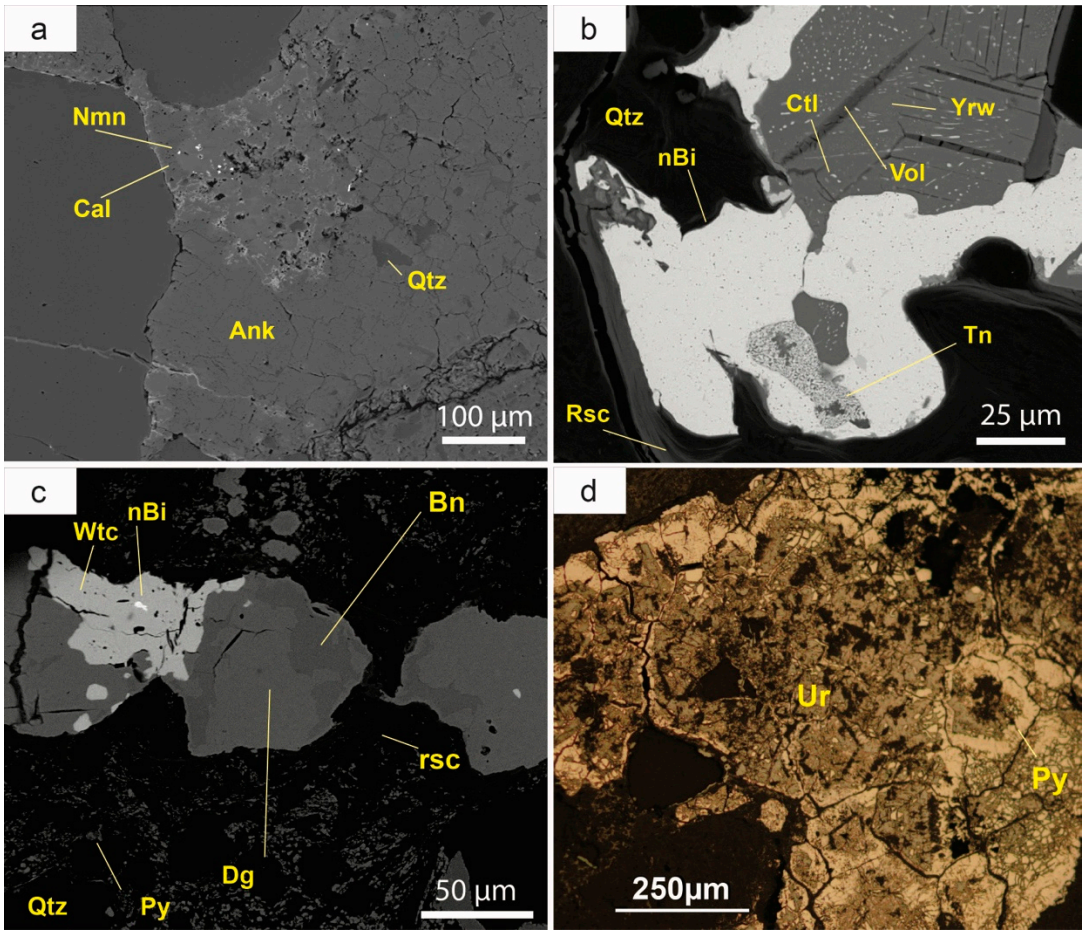

Figure 8. (**a**) Small grains of naumannite (Nmn) scattered in ankerite (Ank) and quartz (Qtz) replacing the early calcite cement (Cal); (**b**) Yarrowite (Yrw) with fine chlausthalite inclusions (Ctl) interstitial to quartz (Qtz) and roscoelite (Rsc). The former is replaced along grain boundaries by symplectitic native bismuth (nBi) with tennantite (Tn) and altered along cleavage by supergene volborthite (Vol); (**c**) Bornite (Bn) replaced by digenite (Dg), followed by native bismuth (nBi) and wittichenite (Wtc). Note pyrite (Py) and quartz (Qtz) in the groundmass; (**d**) Pyrite (Py) replaced along zoning by uraninite (Ur). (a–c) are SEM images, mode BSE; (d) is a reflected light image, in PPL.

5.3.11. Native Bi

Native bismuth is the most common native element in this deposit. It usually occurs as small crystals (10 µm), although it can reach 100 µm in some samples. These grains are frequently subhedral and are associated with copper sulphides. In some cases, native bismuth has been found pseudomorphically replaced by bismuthinite.

5.3.12. Wittichenite [Cu_3BiS_3]

This sulphosalt is scarce in the Eureka mine complex and typically replaces Cu sulphides along with native bismuth (Figure 8c). It usually forms anhedral grains, commonly with a diameter below 100 µm.

5.3.13. Tennantite-Group Minerals [$Cu_6[Cu_4(Fe,Zn)_2]As_4S_{13}$]

Although tennantite-group minerals are rare minerals in the Eureka deposit, they were found in most of the studied occurrences as micrometric grains. They generally replace other ore minerals, mainly Cu sulphides, so they are typically anhedral. In many cases, it is possible to see zoning, with a very wide range in Sb and As compositions, as well as in Ag and Fe. Furthermore, these crystals

incorporate relatively high Bi content, which is very unusual in tetrahedrite. Some grains could be identified as Zn-rich tennantite, a very uncommon mineral worldwide.

5.3.14. Sphalerite [ZnS]

Sphalerite is very rare in this deposit and it has a very small grain size (usually less than some tens of microns). It typically replaces Cu sulphides. In turn, some sphalerite grains are replaced by Zn-rich tennantite. No chalcopyrite disease, a speckling of sphalerite with micron-scale chalcopyrite blebs, has been observed in these crystals. All sphalerite crystals are extremely pure and when analyzed with EMPA show almost nil Fe content. The Cd, In, Ga, Hg, Mn, Cu, and Sn contents are below the detection limits of the microprobe.

5.3.15. Uraninite [UO_2]

This is the most abundant uranium mineral in the Eureka deposit and it forms massive aggregates that can be seen with the naked eye. These black-colored aggregates are some millimeters wide and a few centimeters long. Uraninite is related to coal seams, where it occurs as small nests a few microns in diameter. It can also be found replacing roscoelite or V-muscovite, along cleavage planes. Uraninite is one of the latest minerals that crystallized during the stratabound mineralisation phase, replacing most of the minerals previously mentioned (Figure 8d). In turn, it was locally replaced by very late-forming Cu sulphides and by a large diversity of secondary phases. Therefore, it is generally anhedral. In some cases, it is botryoidal or cryptocrystalline.

5.4. Vein Mineralisation

This style of mineralisation occurs as subvertical veinlets, which cut previously crystallized minerals. The walls of these veins are straight and the filling is symmetric. This indicates that vein formation took place after the rock consolidation (i.e., the cementation of the original red beds). These mineralisations have similarities in mineralogical content and textural patterns with those found in the neck domains of boudins developed in the most competent layers.

The main filling mineral is comb quartz and it occurs as euhedral microcrystalline grains near the boundaries of the veins. Euhedral saddle crystals of ankerite-dolomite, with a characteristic rhombohedral habit, are also abundant and overgrow quartz. These crystals are usually millimetric (and up to 1 cm) and can be zoned. Ankerite is usually altered to fine-grained goethite along cleavage planes. Some grains have a slight manganese enrichment. Sr-poor barite is predominant in some millimeter-wide veinlets found in the vicinity of the deposit. It occurs as platy pale pink crystals, up to 1 cm in length.

In contrast to the stratabound mineralisation, minerals with U, V, Bi, Co, Ni, Sb, Se, or REE have not been identified in the veinlets. Instead, ores are limited to small amounts of bornite, digenite and chalcopyrite. An additional difference with the stratabound mineralisation is the widespread occurrence of galena in these veinlets. Galena occurs commonly on the inner part of the veinlets, either as thin bands (up to 100 μm in width) or as small (<1 mm) isolated crystals. It is not enriched in Sb, Bi, Ag, or Se. It can be replaced by fine-grained bornite (<100 μm) and other Cu sulphides along grain boundaries, cleavage and fissures. Although digenite is the main Cu-sulphide replacing galena and bornite, it is present in very low amounts. In contrast, anhedral chalcopyrite is the main ore mineral in the veins, concentrated at the necking zones of the boudinage structures in the sandstones. Its grain size may reach several millimeters in the Castell-estaó outcrop.

5.5. Mineral Sequence of the Primary Mineralisation

Even excluding the minerals formed during the weathering of this deposit, the mineral sequence is very complex. Therefore, it is difficult to reconstruct the complete sequence, because the mineral associations are not the same in all the sectors of the mineralized lenses. In general, there are different associations in the outer zones of the mineralized lenses, where the early carbonates are preserved,

when compared with the innermost zones, in particular, in the vicinity of organic matter. However, an idealized general mineral sequence has been proposed (Figure 9).

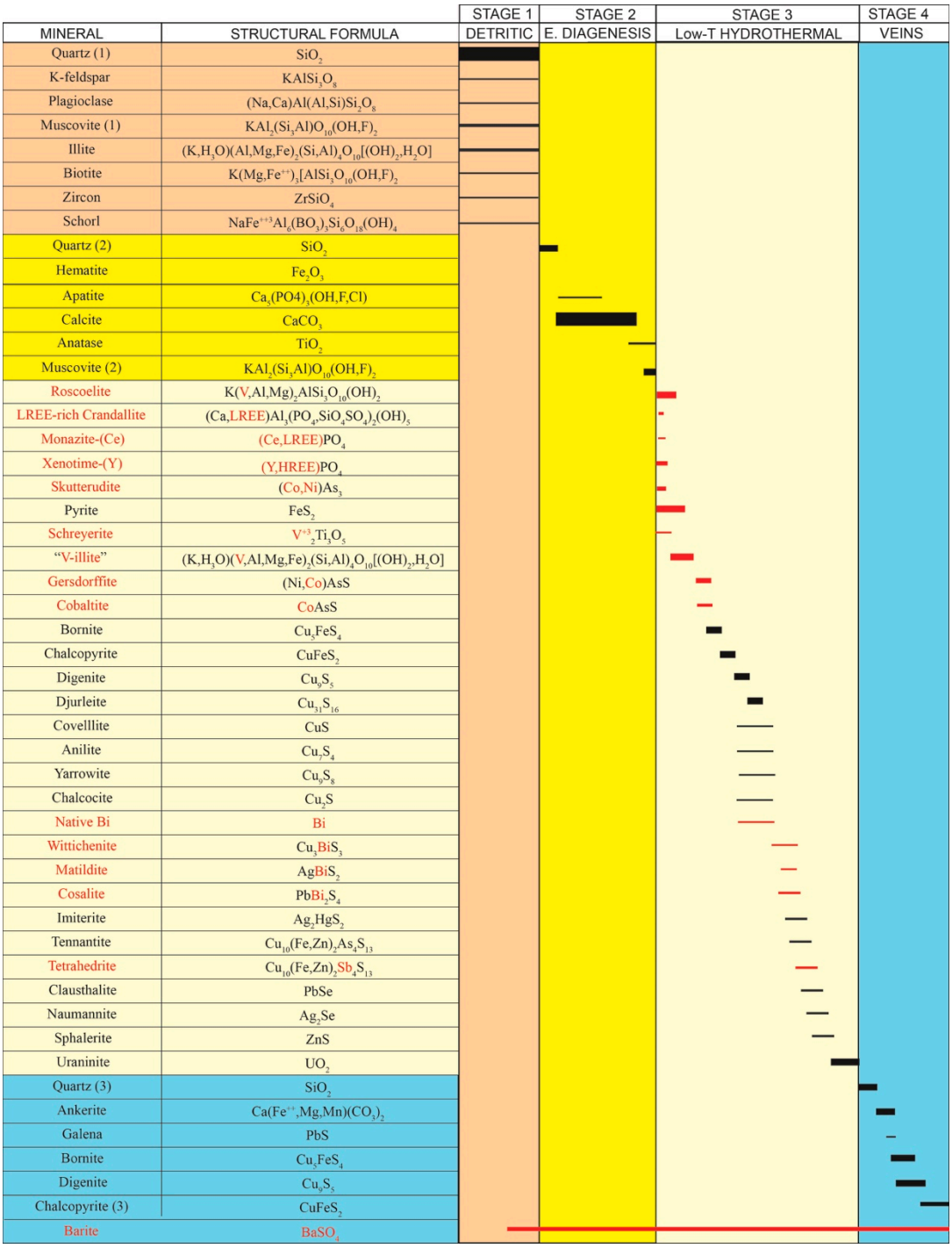

Figure 9. Crystallization sequence of the stratabound and vein mineralisation. Critical metals [22] and the minerals accommodating them are highlighted in red colour. Thickness of the bars indicates the relative abundance of the minerals.

5.6. Supergene Mineralisation

Supergene mineralisation resulted from weathering of the primary stratabound mineralisation (i.e., sulphides, arsenides, selenides, uraninite, and vanadium-rich minerals). This process led to the formation of a wide range of minerals, including vanadates, phosphates, and arsenates, sulphates

and, sporadically, selenites, carbonates and molybdates. Most of these secondary minerals are found as pseudomorphic replacements of primary ores. However, they can also occur as surficial crusts or efflorescences, or fill minor joints and late veinlets that follow schistosity planes or along cleavage planes of micas. These late-forming minerals typically exhibit non-replacive grain boundaries among them, and the mineral successions are usually passive.

Goethite [FeO(OH)] was probably the first mineral to form, as thin botryoidal aggregates, pseudomorphs after sulphides or filling veinlets.

5.6.1. Vanadates of the Carnotite Group

Sengierite [$Cu_2(UO_2)_2(VO_4)_2 \cdot 6H_2O$] is quite abundant in the Eureka deposit and it usually occurs as green micrometric tabular crystals. However, some crystals can be up to few millimeters in length. Sengierite typically crystallizes as radial aggregates, filling vuggy porosity where primary Cu-bearing sulphides have been leached. It can also fill small veinlets. Sengierite replaces carnotite [$K_2(UO_2)_2V_2O_8) \cdot 3H_2O$] and uraninite and is replaced by other secondary copper minerals, like brochantite or chenevixite (Figure 10a).

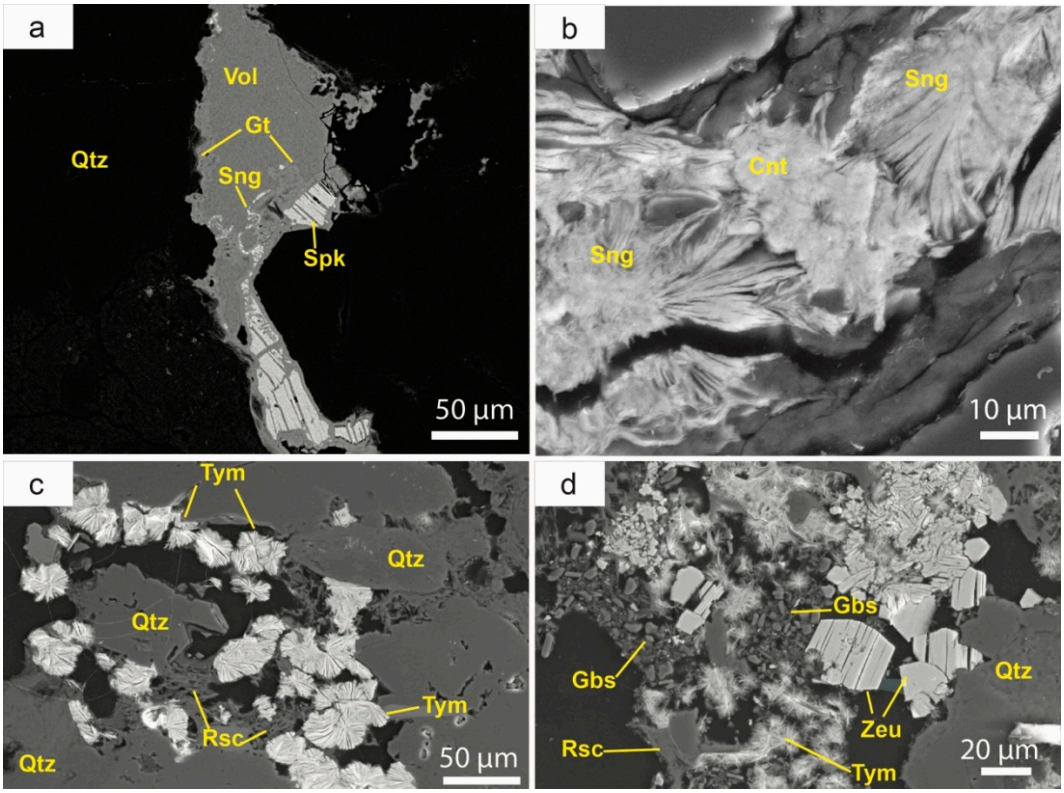

Figure 10. SEM images (BSE mode) showing the textures of the uranyl vanadates of the carnotite group. (**a**) Spionkopite (Spk) in secondary porosity interstitial to detrital quartz (Qtz) and replaced by goethite (Gt), followed by sengierite (Sng) and finally volborthite (Vol) crustiform growths; (**b**) Veinlet in roscoelite with sengierite (Sng) replaced by carnotite (Cnt); (**c**) Vuggy porosity in detrital quartz (Qtz) and roscoelite (Rsc), filled by tyuyamunite (Tym); (**d**) Secondary porosity in quartz and roscoelite filled by gibbsite (Gbs) and tyuyamunite platelets (Tym), followed by zeunerite (Zeu).

Tyuyamunite [$Ca(UO_2)_2(VO_4)_2 \cdot 5–8H_2O$] and carnotite crystallized during late weathering pulses, as they may overgrow grains of the copper-uranium arsenate (zeunerite). They are widely spread in this deposit, as small (<100 µm) yellow tabular crystals (Figure 10b–d) that either pseudomorph primary uranium minerals or fill small veinlets along cleavage planes of early vanadium-rich micas.

Vanuralite [$Al(UO_2)_2(VO_4)_2(OH)\cdot 11H_2O$] is the least abundant member of the group, and has been found replacing roscoelite, in radial groups smaller than 50 μm.

5.6.2. Other Vanadates

Volborthite [$Cu_3(V_2O_7)(OH)_2\cdot 2H_2O$] is widespread in the deposit. It forms fine-grained radial aggregates of tabular crystals, commonly replacing roscoelite along cleavage (Figure 11a), although it also occurs in veinlets, where it overgrows other arsenates and vanadates. Uvanite [$U_2V^{5+}{}_6O_{21}\cdot 15(H_2O)$] has been found as radial aggregates in detrital quartz porosity, together with brochantite (Figure 11b).

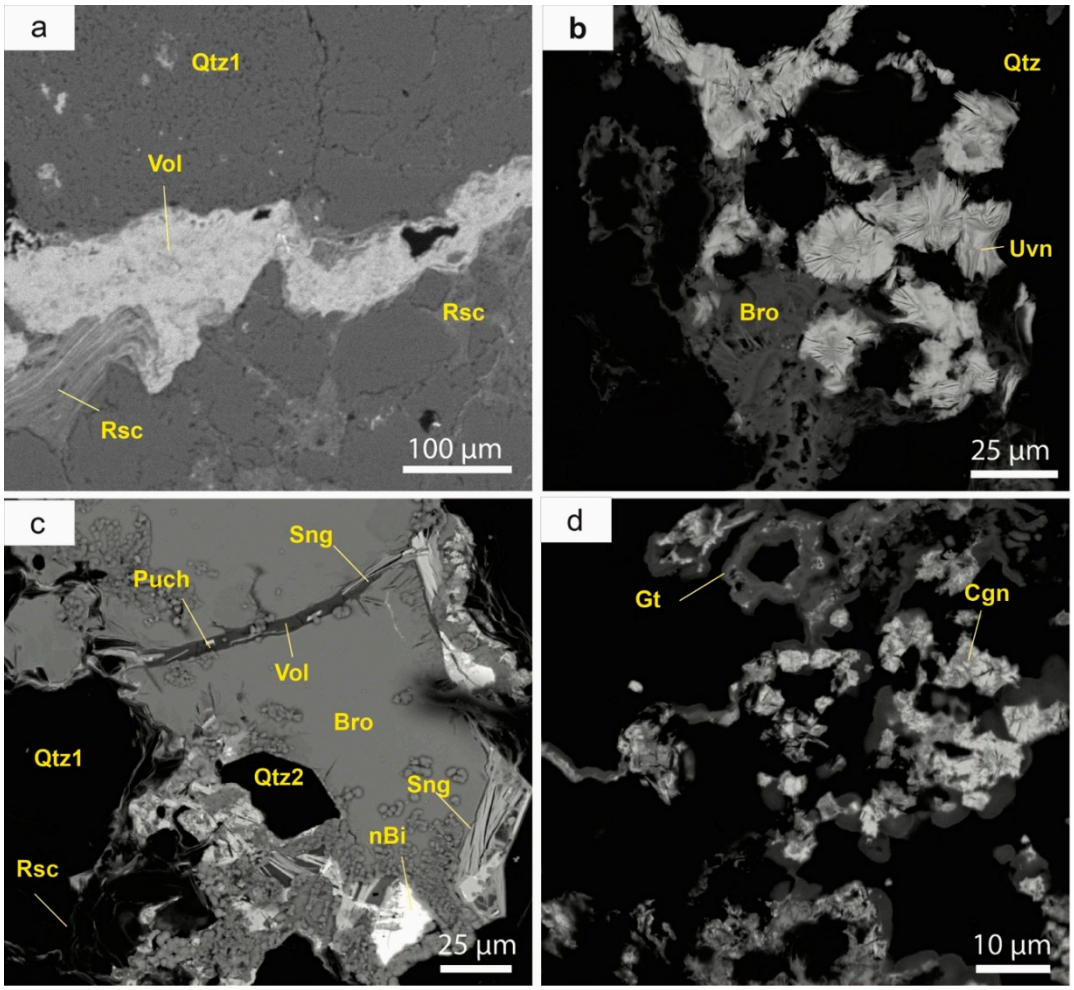

Figure 11. SEM-BSE images of secondary vanadates of the Eureka mine. (**a**) Detrital quartz (Qtz1) and interstitial roscoelite (Rsc) veined by volborthite (Vol). Note replacement of roscoelite along cleavage; (**b**) Radial aggregations of uvanite (Uvn) associated with brochantite (Bro) in secondary porosity among detrital quartz (Qtz); (**c**) Copper sulphide, with native bismuth inclusions (nBi), pseudomorphosed by brochantite (Bro) and sengierite (Sng); late veinlets filled with volborthite (Vol), sengierite (Sng) and pucherite (Puch) cut the ensemble, with syntaxial quartz cement (Qtz2); (**d**) Intergrowths of compreignacite (Cgn) with goethite (Gt), probably replacing a primary association of pyrite and uraninite (compare with the Figure 8d).

Pucherite [$Bi(VO_4)$] has been found as a pseudomorph of native bismuth and as euhedral crystals filling small cracks, along with sengierite and volborthite (Figure 11c). Small (few microns) spherulitic growths filling porosity where the primary mineralisation has been extensively replaced have been tentatively classified as vanuranylite [$(H_3O)_2(UO_2)_2(VO_4)_2\cdot 4H_2O$].

5.6.3. Uranyl Oxyhydroxides

Compreignacite [$K_2(UO_2)_6O_4(OH)_6{\cdot}7H_2O$] occurs as yellowish botryoidal aggregates that could be pseudomorphs after uraninite. It is commonly intergrown with goethite (Figure 11d).

5.6.4. Phosphates and Arsenates of the Autunite Group

Zeunerite [$Cu(UO_2)_2(AsO_4)_2{\cdot}12H_2O$] and metazeunerite [$Cu(UO_2)_2(AsO_4)_2{\cdot}8H_2O$] are the most common minerals of the autunite group found in the Eureka mine. They form euhedral crystals with a tabular habit up to few millimeters long. They are commonly arranged in radial aggregates, filling small cracks along the slaty cleavage (Figure 12a) or pseudomorphing copper sulphides (Figure 12b). Other arsenates of the group, such as kahlerite [$Fe(UO_2)_2(AsO_4)_2{\cdot}12H_2O$], occur as tabular crystals (<40 μm) in radial groups pseudomorphing gersdorffite near uraninite and digenite.

Phosphates of the autunite group such as autunite [$Ca(UO_2)_2(PO_4)_2{\cdot}11H_2O$] and torbernite [$Cu(UO_2)_2(PO_4)_2{\cdot}12H_2O$] are very unusual in the Eureka mine. When present, they form small (<100 μm) euhedral platy crystals, which commonly fill open cracks (Figure 12c). The occurrence of the dehydrated counterparts in Eureka (metaautunite and metatorbenite) cannot be ruled out.

5.6.5. Uranyl Selenites

Uranyl selenites as guilleminite [$Ba(UO_2)_3(SeO_3)_2O_2{\cdot}3H_2O$], haynesite [$(UO_2)_3(SeO_3)_2(OH)_2{\cdot}5H_2O$] and demesmaekerite [$Pb_2Cu_5(UO_2)_2(SeO_3)_6(OH)_6{\cdot}2H_2O$], very rare worldwide, have been found in this deposit as tabular crystals a few microns long (Figure 11a). They usually occur inside small veinlets, developed through the slaty cleavage and replacing roscoelite following its cleavage (Figure 12b). They have also been found pseudomorphing minerals of the chalcocite group (Figure 12c).

5.6.6. Uranyl Carbonates

Uranyl carbonates are very rare in the Eureka deposit, but some crusts of fine-grained agricolaite [$K_4(UO_2)(CO_3)_3$] are found as replacement of sulphides near the surface outcrop adjacent to Castell-estaó, along with malachite, probably as pseudomorphs after copper sulphides (Figure 13a). Andersonite [$Na_2Ca(UO_2)(CO_3)_3{\cdot}6H_2O$] and čejkaite [$Na_4(UO_2)(CO_3)_3$] intergrowths crystallized as tiny efflorescences on the walls of mine tunnels [2].

5.6.7. Uranyl Sulphates

Uranyl sulphates are very rare in the Eureka deposit and are typically found filling secondary porosity produced during weathering of sulphides associated with uraninite. Johannite [$Cu(UO_2)_2(SO_4)_2(OH)_2{\cdot}8H_2O$] usually forms radial aggregates less than 50 μm in diameter, overgrown by malachite [$Cu_2(CO_3)(OH)_2$] and other secondary minerals of copper. However, it can also occur in veinlets near mixtures of sulphides and uraninite. Scarce radial aggregates of uranopilite/meta-uranopilite [$(UO_2)_6(SO_4)O_2(OH)_6{\cdot}14H_2O$] also formed after these secondary Cu minerals. Poorly developed natrozippeite [$Na_5(UO_2)_8(SO_4)_4O_5(OH)_3{\cdot}12H_2O$] efflorescences have also been described on the outcropping surfaces [2].

5.6.8. Uranyl Silicates

Uranyl silicates are rare in the Eureka mine. Uranophane [$Ca(UO_2)_2SiO_3(OH)_2{\cdot}5H_2O$] is the most abundant uranyl silicate and it forms radial groups of fibrous crystals (<50 μm in length) (Figure 13b), generally associated with secondary copper carbonates. Kasolite [$Pb(UO_2)[SiO_4]{\cdot}H_2O$] has been tentatively identified as fine-grained aggregates intergrown with botryoidal delafossite [$CuFeO_2$], probably as a replacement of an association of sulphides. Cuprosklodowskite [$Cu(UO_2)_2(SiO_2OH)_2{\cdot}6H_2O$] radial aggregates are common as pseudomorphs after copper sulphides, along with other secondary minerals (Figure 13c). Boltwoodite [$HK(UO_2)(SiO_4){\cdot}1.5(H_2O)$] occurs as tiny veinlets of

centimetric continuity, generally following the slaty cleavage developed in vanadium micas. It forms fibrous crystals, arranged in radial aggregates (Figure 13d).

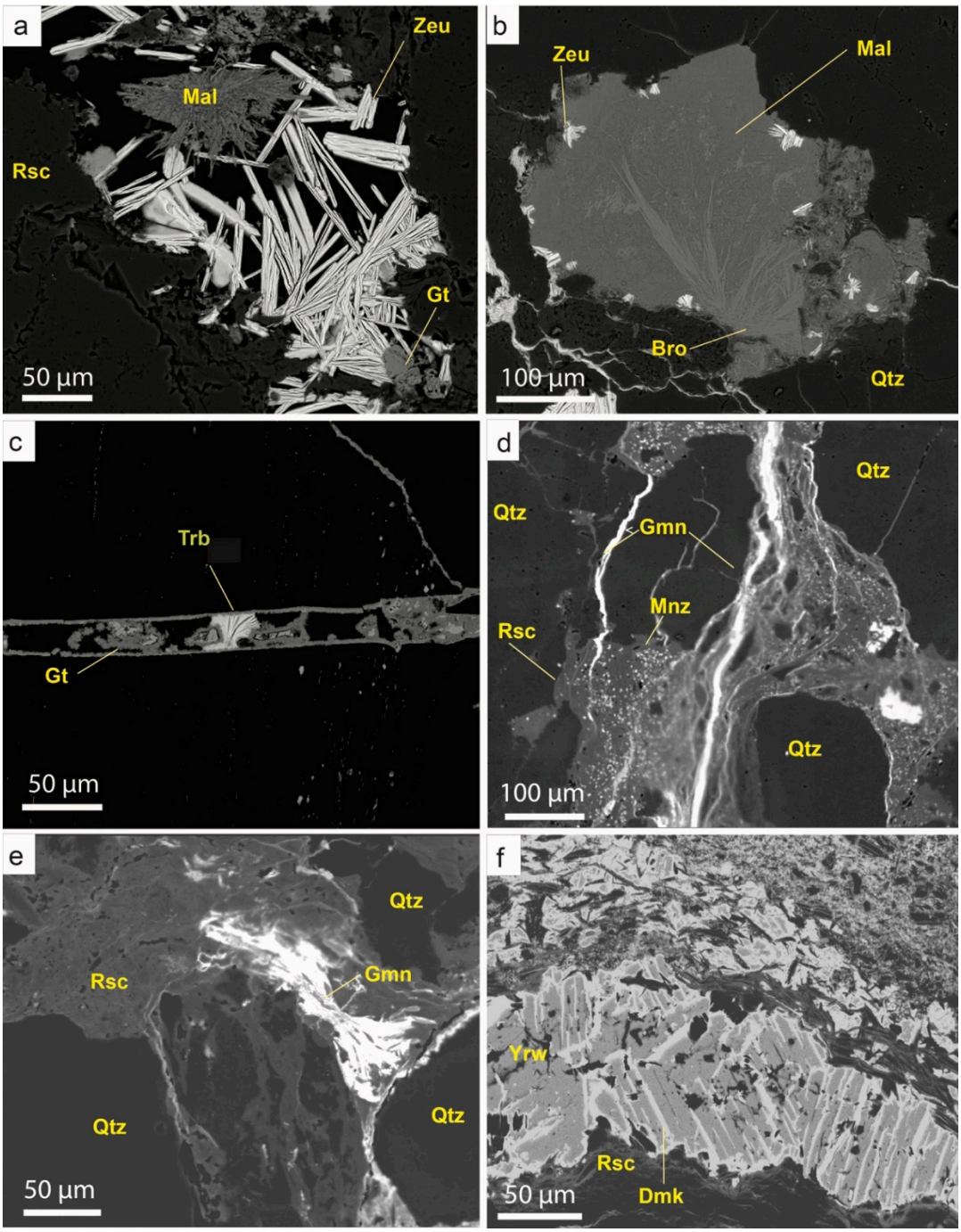

Figure 12. SEM-BSE images of showing the main phosphates and arsenates of the autunite group, as well as some of the uranyl selenites found in the Eureka mine. (**a**) Boxwork filling with goethite (Gt), tabular crystals of zeunerite/metazeunerite (Zeu) and malachite (Mal); (**b**) Full replacement of a copper sulphide by zeunerite/metazeunerite (Zeu), brochantite (Bro) and malachite (Mal) in detrital quartz (Qtz); (**c**) Vein infilling with goethite (Gt) followed by torbernite (Trb); (**d**) Veinlets with guilleminite (Gmn) in roscoelite (Rsc) with monazite disseminations (Mnz); (**e**) Guilleminite (Gmn) replacing roscoelite (Rsc) in detrital quartz (Qtz); (**f**) yarrowite crystals (Yrw) replaced along twinning planes, grain boundaries and cleavage by demesmaekerite (Dmk). Note that roscoelite (Rsc) is arranged along the slaty cleavage.

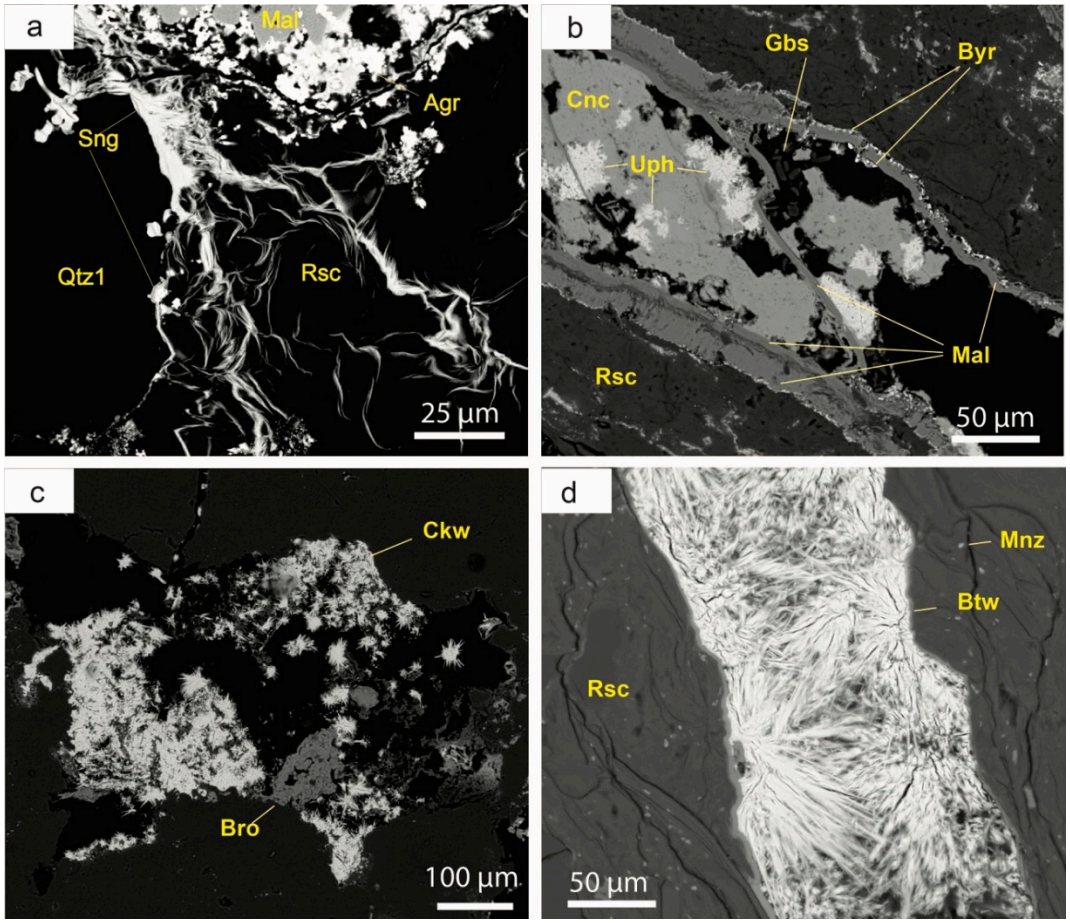

Figure 13. SEM-BSE images of late supergene uranyl carbonates and uranyil silicates. (**a**) Agricolaite (Agr) and malachite (Mal) as pseudomorphs after a sulphide grain. The roscoelite (Rsc) near detrital quartz (Qtz1) is replaced along cleavage by sengierite (Sng); (**b**) Sequence of vein infilling in roscoelite (Rsc) with malachite (Mal) followed by beyerite (Byr), then gibbsite (Gbs) and uranophane (Uph) followed by conichalcite (Cnc); (**c**) Radial aggregates of cuprosklodowskite needles (Ckw) pseudomorphing copper primary ores, together with brochantite (Bro); (**d**) Boltwoodite (Btw) in radial aggregates filling a veinlet in roscoelite (Rsc). Note the widespread occurrence of small monazite crystals (Mnz) scattered in roscoelite.

5.6.9. Other Supergene Minerals

The list of the accessory supergene minerals in the Eureka deposit is very long (Figure 14). Most of them occur as crusts over the outcrops or are found as late phases (i.e., late vein infilling or pseudomorphs). The most common minerals are copper carbonates such as malachite and azurite, although beyerite [$Ca(BiO)_2(CO_3)_2$] has also been identified. Malachite [$Cu_2(CO_3)(OH)_2$] and azurite [$Cu_3(CO_2)(OH)_2$] typically occur as thin, cryptocrystalline crusts, although they may also be found as vein-infilling phases (Figure 13b). Beyerite is a bismuth carbonate that crystallized early in the mineral sequence, as pseudomorphs after native bismuth. It forms very small (<10 µm) elongate crystals, sometimes arranged in radial groups, typically on the walls of small cracks (Figure 13b). Bismite [Bi_2O_3] is a pseudomorph of native bismuth and bismuthinite, and it occurs as white cryptocrystalline aggregates.

Copper sulphates, like brochantite [$Cu_4(SO_4)(OH)_6$] or posnjakite [$Cu_4(SO_4)(OH)_6{\cdot}H_2O$], also represent a significant amount of the supergene minerals in the Eureka deposit. Brochantite occurs as very small crystals (tens of microns) with a tabular or prismatic habit. It is usually pseudomorphic of

Cu sulphides, but it can also fill small micrometric veinlets. Posnjakite formed as very late incrustations on the walls of the trenches.

Additionally, arsenates like conichalcite [$CaCu(AsO_4)(OH)$] or chenevixite [$Cu_2Fe^{3+}{}_2(AsO_4)_2(OH)_4$] are also abundant in this locality. Conichalcite often occurs as pseudomorph of tennantite and also forms fine yellowish green crusts over the outcrops. Chenevixite occurs as cryptocrystalline spherulitic aggregates, which replace many of the earlier Cu sulphide minerals and sometimes overprint sengierite. Chenevixite can also fill vuggy porosity.

MINERAL	STRUCTURAL FORMULA	STAGE 5 SUPERGENE
Goethite	$FeO(OH)$	
Beyerite	$Ca(BiO)_2(CO_3)_2$	
Compreignacite	$K_2(UO_2)_6O_4(OH)_6 \cdot 7H_2O$	
Barite	$BaSO_4$	
Vanuralite	$Al(UO_2)_2(VO_4)_2(OH) \cdot 11H_2O$	
Brochantite	$Cu_4(SO_4)(OH)_6$	
Antlerite	$Cu_3(SO_4)(OH)_4$	
Azurite	$Cu_3(CO_3)_2(OH)_2$	
Malachite	$Cu_2(CO_3)(OH)_2$	
Wulfenite	$PbMoO_4$	
Anglesite	$PbSO_4$	
Mimetite	$Pb_5(AsO_4)_3Cl$	
Johannite	$Cu(UO_2)_2(SO_4)_2(OH)_2 \cdot 8H_2O$	
Zeunerite	$Cu^{++}(UO_2)_2(AsO_4)_2 \cdot 10\text{-}16H_2O$	
Kahlerite	$Fe(UO_2)_2(AsO_4)_2 \cdot 12H_2O$	
Natrouranospinite	$(Na_2Ca)(UO_2)_2(AsO_4)_2 \cdot 5H_2O$	
Conichalcite	$CaCu(AsO_4)(OH)$	
Chenevixite	$Cu_2Fe^{+++}{}_2(AsO_4)_2(OH)_4$	
Gibbsite	$Al(OH)_3$	
Uranophane	$Ca(UO_2)_2(SiO_3)(OH)_2 \cdot 6H_2O$	
Cuprosklodowskite	$Cu(UO_2)_2(HSiO_4)_2 \cdot 6H_2O$	
Kasolite	$Pb(UO_2)SiO_4 \cdot H_2O$	
Volborthite	$Cu^{++}{}_3V^{+++++}{}_2O_7(OH)_2 \cdot 2H_2O$	
Sengierite	$Cu_2(UO_2)_2V_2O_8 \cdot 6H_2O$	
Carnotite	$K_2(UO_2)_2V_2O_8 \cdot 1\text{-}3(H_2O)$	
Tyuyamunite	$Ca(UO_2)_2V_2O_8 \cdot 1\text{-}3(H_2O)$	
Pucherite	$BiVO_4$	
Autunite	$Ca(UO_2)_2(PO_4)_2 \cdot 10\text{-}12H_2O$	
Torbernite	$Cu(UO_2)_2(PO_4)_2 \cdot 8\text{-}12H_2O$	
Metaankoleite	$K_2(UO_2)_2(PO_4)_2 \cdot 6H_2O$	
Demesmaekerite	$Pb_2Cu_5(UO_2)_2(SeO_3)_6(OH)_6 \cdot 2H_2O$	
Guilleminite	$Ba(UO_2)_3(SeO_3)_2O_2 \cdot 3H_2O$	
Haynesite	$(UO_2)_3(SeO_3)_2(OH)_2 \cdot 5H_2O$	
Posnjakite	$Cu_4(SO_4)(OH)_6 \cdot (H_2O)$	
Uranopilite	$[(UO_2)_6(SO_4)O_2(OH)_6(H_2O)_6] \cdot 8H_2O$	
Erythrite	$Co_3(AsO_4)_2 \cdot 8H_2O$	
Annabergite	$Ni_3(AsO_4)_2 \cdot 8H_2O$	
Natrozippeite	$Na_5(UO_2)_8(SO_4)_4O_5(OH)_3 \cdot 12H_2O$	
Andersonite	$Na_2Ca(UO_2)(CO_3)_3 \cdot 6H_2O$	
Čejkaite	$Na_4(UO_2)(CO_3)_3$	

Figure 14. Crystallization sequence of the secondary minerals of the Eureka mine, indicating the minerals of critical elements [22] in red. Width of the lines are proportional to the modal abundance of the mineral in the deposit.

5.7. Recent Mineralisation

Some minerals occur as very thin crusts or efflorescences at the trenches of the surface outcrops or on the walls of the underground tunnels, thus indicating a recent (<60 years) formation (Figure 14). These aggregates rarely contain crystals larger than one millimeter, and they are usually cryptocrystalline. Previous studies have shown that these aggregates are made of oxidized water-rich phases, including posnjakite, uranopilite [$(UO_2)_6(SO_4)O_2(OH)_6{\cdot}14H_2O$], erythrite [$Co_3(AsO_4)_2{\cdot}8H_2O$], annabergite [$Ni_3(AsO_4)_2{\cdot}8H_2O$], abellaite [$NaPb_2(CO_3)_2(OH)$] [3,54] and some rare uranium minerals as natrouranospinite [$(Na_2,Ca)(UO_2)_2(AsO_4)_2{\cdot}5H_2O$], andersonite [$Na_2Ca(UO_2)(CO_3)_3{\cdot}6H_2O$] and čejkaite $Na_4(UO_2)(CO_3)_3$ [2].

Despite Co (and, to a lesser extent, Ni) being common in the primary ores, their weathering products are very rare in the secondary mineral associations of the studied deposit. Erythrite has been found as small powdery efflorescences in the outcrop near Castell-estaó. Annabergite has not been identified.

6. Discussion

The Eureka deposit has been historically classified as a Cu–U–V stratabound deposit hosted in a red-bed [1]. In this deposit, the reducing agent that led to the epigenetic concentration of uranium could be either: i. the plant remnants of the hosting sandstones; or ii. the organic matter from the underlying Silurian shales. However, the plant remnants should be the most feasible geochemical trap in Eureka, because the veins do not contain U–V mineralisation. The association of the deposit with the Alpine deformation and low-grade metamorphism suggests that the deposit could fit better in the metamorphite group of the IAEA [7]. However, the low-grade metamorphism in the Eureka case and the mineralogical and textural similarities with the typical Colorado Plateau deposits allow some comparisons.

Besides uranium, most Redox Sensitive Elements (RSE) (S, N, Fe, P, Mo, As, V, Sb, Se, Ni, Co, Cu and Cr) were also found in the Castell-estaó stratabound mineralisation, resulting in a wide diversity of mineral phases. These elements have been used as geochemical pathfinders for U exploration [55]. In this section, the sources of these elements, as well as the different mineralisation stages and the inferred conditions of formation of the deposit are discussed.

6.1. Sources of Sulphur and Metals

Although the sources of sulphur and metals of the Eureka mine could not be fully constrained, their most plausible origins are discussed next. The evaporites of the Keuper facies are a large reservoir of sulphur and thus a potential source for the Eureka mine deposit. Since they are the detachment level of the main thrust structures in the Pyrenees, it is very likely that large amounts of sulphur could be transported during the multiple episodes of tectonic activity that affected the area. In most uranium-sandstone deposits, sulphur is transported as sulphate and is reduced to H_2S by organic matter or oil [56–58], although in some cases the participation of magmatic fluids has been invoked (i.e., in the Ordos basin in China; [59]). The occurrence of barite in cements and veinlets in the red beds surrounding the Eureka mineralized lenses can be related to the entrance of these sulphate solutions in non-reducing sediments; barite is also described in similar context in many sandstone uranium deposits (for example, [60]).

The sources of the metals can be very diverse, and most of the attention has been focused historically on uranium. The source of uranium in sedimentary deposits has been previously linked to hydrothermal leaching of U-bearing volcanic rocks [61]. This process generates fluids with U and V as uranyl (UO_2^{2+}) and vanadyl (VO^{2+}), two highly soluble complexes. Other authors indicate that U could be supplied directly from hydrothermal fluids heated by the volcanism [62]. However, this hypothesis is at odds with the age of the magmatism, which is older than the Alpine mineralisation of the Eureka mine. Finally, other authors [58,63–65] propose intrabasinal sources for U, in pre-existing

Fe–Ti oxides. The first hypothesis fits the geological setting of Eureka, since calc-alkaline volcanic episodes (Erill-Castell formation) took place in the Carboniferous. These series are unconformably overlain by the Permo-Triassic rocks, not far from the Eureka deposit [30]. Moreover, although there is evidence for Ti remobilization in Eureka, as the presence of schreyerite indicates, the Ti minerals are not very common in the series and their U contents are below the detection limit of the SEM-EDS. Therefore, the hypothesis of the continental series as a source for U can be ruled out in the Eureka case. Instead, it is most likely that the source of uranium is either the volcanoclastic series of the Erill-Castell or the Silurian black shales.

Many authors suggest different sources for U and the other metals [66]. The source of the HFSE (High Field Strength Elements) is here related to the Silurian black shales, which are the detachment level of many main thrusts in the Pyrenees [67]. These shales have been previously described as regional reservoirs of base metals and HFSE sulphides in other domains of the Pyrenees and the Catalonian Coastal Ranges [68,69]. This is consistent with the typical enrichment in V and HFSE in black shales worldwide [70–72] and in oils [73,74]. However, high Sc and Cr contents as those found in some vanadium deposits associated with thrusting [53] have not been observed in Eureka. Black shales often concentrate these elements [75], so their absence in the deposit is better explained by the nonexistence of large volumes of basic or ultrabasic rocks in the thrusted stacking sequence. This interpretation is also consistent with the lack of gold and PGE-bearing minerals in Eureka, in contrast with many deposits associated with shearing [76].

6.2. Deposit Formation

The detailed textural and mineralogical characterisation presented here highlights the complexity of the mineral sequence of the Eureka mine. Moreover, the mineral assemblages identified near the coal seams (i.e., highly mineralised levels) clearly differ from those of the outer zones of the outcrop, where the early carbonates are still preserved. As a consequence, it has been difficult to reconstruct the entire crystallization sequence because the whole assemblage could not be found in the same location. Based on the textural relationships between the different phases, a general mineral sequence is proposed, including both primary (Figure 9) and secondary minerals (Figure 14). From the study of mineral phases and their textural relationships, 5 stages in the development of the deposit are proposed, each one resulting from different genetic conditions.

6.2.1. Stages 1 and 2: Sedimentation and Early Diagenesis

First and second stages include the sedimentation and the lithification of the rock, as well as the formation of calcite cement. The roundness of the quartz grains (Figure 5), together with a poor sorting of sediments, suggests a high-energy depositional environment and/or deposition relatively close to the source area. Moreover, several cycles of sedimentary layers with erosive contacts and a fining-upwards sequence (conglomerate to mudstone) classify the host rocks as alluvial deposits.

6.2.2. Stage 3: Stratabound Mineralisation

This is the primary Cu–V–U mineralisation of the Eureka mine deposit, formed by the interaction of hydrothermal fluids rich in metals with the reducing trap caused by the coal seams interbedded with the sediments (Figure 4b,c). Although these coal seams do not represent more than 1% in volume of the deposit, it has been proved that 0.5 wt % of lignite is enough to form a V–U deposit by reduction of V^{5+} and U^{6+} [77].

Transition metals (and Ba) are effectively transported as chloride complexes in diagenetic and hydrothermal fluids [78], whereas sulphur is commonly transported as sulphate (SO_4^{2-}) complexes during the formation of sandstone-type uranium deposits [58] and many low-temperature hydrothermal deposits [79]. Sulphate complexes can also be effective in the transport of uranium and other critical elements [80,81]. The arrival of hydrothermal fluids to the coal-rich reducing domains triggered a

massive precipitation of Cu–V–U-rich minerals, including silicates, sulphides, arsenides and selenides in Eureka.

V^{5+} was reduced to V^{3+} and was incorporated in the structure of sheet silicates, forming roscoelite and V-rich illite, as well as oxides (schreyerite). However, part of the V in roscoelite could be tetravalent, according to experiments [82].

Previous experimental works have shown that hydrothermal transportation of REE as SO_4^{2-} complexes is very effective [83,84]. The reduction of SO_4^{2-} and the precipitation of sulphides$^-$ in the reducing front would trigger an extensive precipitation of the REE minerals. In Eureka, the formation of REE-bearing phosphates (i.e., monazite and xenotime) is interpreted as the result of the interaction of REE-enriched hydrothermal fluids with phosphates derived from de-stabilization of organic matter [85].

Similarly, SO_4^{2-} was quickly reduced to H_2S leading to the formation of a wide variety of Cu and Fe sulphides. These fluids initially had a high S activity, as it is shown by the replacement of the hematite cement and the precipitation of abundant pyrite and bornite in the early stage of the stratabound mineralisation.

Selenium mostly formed selenides (Figure 8a,b), but significant Se contents have also been found in sulphides, mainly in covellite (up to 2.8 wt %) and minerals of the chalcocite group (up to 0.4 wt %). [86] proposed that the ratio Cu/Se remains constant during Cu leaching between chalcocite and covellite. However, the occurrence of selenium minerals as admixtures in some sulphides (Figure 8b), coupled with the low Se contents in most of the analysed copper minerals, suggests that low-temperature Pb–Zn rich fluids could remobilize part of the selenium of minerals of the chalcocite group and covellite towards chlausthalite and naumannite.

Uranium mostly precipitated as uraninite, a very insoluble mineral in a reducing environment. Although [87] pointed out that U^{4+} can be soluble under low-pH conditions and high temperature, the maximum temperature achieved during the metamorphism is probably on the order of 250 °C and the pH could be buffered towards neutral during the reaction of the acidic fluids with the carbonate cements of the sandstone.

6.2.3. Stage 4: Vein Mineralisation

This is represented by small veinlets, as well as the mineralised necking zones of the boudinage structures observed in the host sandstones (Figure 4d,e). In both cases, they are related to syntectonic hydrothermal processes that took place during the main Alpine compression phase.

The symmetric filling of most of the veinlets indicates that their formation took place later than the consolidation of the rock and, by extension, subsequently to the cementation of the original red bed. These mineralized veinlets predate or are synchronous with the Alpine deformation, as they are cut and moved by layer-to-layer slide (Figure 4e). This type of sliding could be related to back- thrusting or to flexural slip folds [51].

In contrast to the stratabound mineralisation, veins are poorly mineralised, with only minor amounts of sulphides (i.e., bornite, chalcopyrite, digenite, galena). These mineralogical differences could be related to changes in the composition of the mineralizing fluids, resulting from fluid flow during different stages of the orogenic process. However, it is most likely that the lack of organic matter in the veins or in the hosting sandstones is responsible for the absence of significant RSE in the veins. This mineralisation style could thus represent the different behavior of the same mineralizing fluids in more incompetent beds devoid of large volumes of organic matter.

6.2.4. Stage 5: Supergene Mineralisation

This stage is characterized by the development of pseudomorphs, crusts and efflorescences of selenites, phosphates, arsenates, sulphates, carbonates and vanadium oxysalts. Most minerals are found directly on the weathered profile, thus suggesting a low mobility for these elements under oxidizing conditions. It is symptomatic that most V oxysalts are found in the immediate vicinity of the roscoelite-rich groundmass, typically replacing it along the cleavage. The irregular

distribution of the complex primary ores and gangues in the deposit, along with the modifications of the pH and Eh in the weathering profile, explain the extreme diversity of mineral species, which is probably far from being completely described (Figure 14). Hence, the Eureka mine is a good natural laboratory to study the behavior of these elements in low-temperature environments controlled by reduction-oxidation processes.

Vanadium oxysalts are the most common products of supergene enrichment in the deposit, which is unsurprising considering the wide distribution of roscoelite in the Eureka mine. Pervasive alteration of roscoelite is explained here by interaction of this mica with the sulphuric solutions resulting from the simultaneous alteration of sulphides. This interpretation is consistent with the simultaneous precipitation of sulphates and vanadium oxysalts (Figure 11). These minerals are found either directly associated with the primary ores, in veins or as surface crusts. The mineral distribution suggests that the oxidized vanadium species occur near the surface. Although a diversity of V-bearing minerals exists in Eureka, only V^{5+} species are found as secondary products. V^{4+} minerals such as montroseite [88], common in sandstone-type deposits (i.e., the Colorado Plateau; [89,90]), are absent in the Eureka mine. The predominance of uranyl vanadates is a distinctive feature of this deposit. In contrast, the weathering profiles of vein uranium deposits typically lack V phases and the U parageneses are dominated by arsenates, sulphates and phosphates (e.g., in Jáchimov, Czech Republic; [91]).

Uraninite alteration led to a wide diversity of minerals. The most common secondary products of U in Eureka are uranyl phosphates, arsenates, vanadates and, to a lesser extent, selenites, sulphates and carbonates. Sulphates are rare in this deposit, probably due to their high solubility [92]. Carbonates are found in the tunnel walls, which indicates that uranyl was transported in solution by highly soluble carbonate complexes [93,94]. Release of silica and aluminium during roscoelite alteration may also explain the formation of gibbsite and uranium silicates (i.e., botwoodite, uranophane, cuprosklodowskite, kasolite). These silicates predominate in the early stages of weathering under alkaline or neutral pH conditions [93,94]. The occurrence of uranophane also requires a neutral pH [92]. Pervasive sulphide alteration of the primary deposit would thus explain the low abundance of uranophane in Eureka. Moreover, the resulting fluids had a lower pH, thus favoring the formation of U^{6+} phosphates, arsenates and vanadates in later stages of the mineralisation [93,94]. Among these, carnotite and tyuyamunite can be used to define the pH conditions of formation in the outer part of the weathered zone. Although historically it had been considered that these minerals typically crystallized under alkaline conditions and only very rarely at pH < 6 [77,78] –unless rauvite was present [95]–, recent studies have shown that they can easily form under slightly acidic environments (pH = 5.5–7) [94,96,97]. A shift towards slightly acidic conditions in Eureka is consistent with mineralizing fluids affected by extensive sulphide alteration.

The mineralogy of the vanadium oxysalts largely depends on the chemistry of the minerals accompanying roscoelite. Alteration of uranite-roscoelite associations could directly precipitate carnotite. In Eureka, tyuyamunite is less abundant than carnotite, probably because its formation requires higher activity of Ca with respect to K and most of the vanadium oxysalts are produced by alteration of roscoelite, which is a K mica. Hence, the formation of tyuyamunite could only happen by destabilization of calcite in the outer part of the deposit.

Arsenides and sulpharsenides of Ni–Co are very common in the deposit and are easily altered to a variety of arsenates. Since Cu is also very common in the primary association, it is not surprising that the most abundant uranyl arsenate is zeunerite [$Cu^{2+}(UO_2)_2(AsO_4)_2{\cdot}10–16H_2O$], whereas kahlerite ($Fe(UO_2)_2(AsO_4)_2{\cdot}12H_2O$) or natrouranospinite ($(Na_2Ca)(UO_2)_2(AsO_4)_2{\cdot}5H_2O$) are rarely found in the Eureka deposit. Ni and Co arsenates (i.e., erythrite and annabergite) are found as efflorescences on the surface of the deposit (mainly erythrite), which highlights the mobility of these elements in the weathering profile.

The products of alteration of selenides are confined to the deepest parts of the profile, in the limit of the reduction front. Weathering of selenium-bearing minerals, including the minerals of the chalcocite group, results in diverse uranyl selenites, such as guilleminite $Ba(UO_2)_3(SeO_3)_2O_2{\cdot}3H_2O$, haynesite

($(UO_2)_3(SeO_3)_2(OH)_2{\cdot}5H_2O$) and demesmaekerite ($Pb_2Cu_5(UO_2)_2(SeO_3)_6(OH)_6{\cdot}2H_2O$). However, no selenates were formed. Therefore, in contrast with other elements such as Mo and As, selenium is quite immobile and does not move to the highest parts of the weathering profile where selenates could be formed. Similar uranyl selenites are also relatively common in the weathering profile of Cu–(U) deposits when the primary ores contain selenides or Se-rich sulphides, as in the Central African Copper Belt in Katanga, Congo [98].

Apatite alteration provides the PO_4 necessary to form secondary uranyl phosphates of the autunite and meta-autunite groups such as autunite ($Ca(UO_2)_2(PO_4)_2{\cdot}10–12H_2O$), torbernite ($Cu(UO_2)_2(PO_4)_2{\cdot}8–12H_2O$) and metaankoleite ($K_2(UO_2)_2(PO_4)_2{\cdot}6H_2O$). However, the scarcity of apatite in Eureka makes these phosphates very rare in this locality, in contrast with their usual abundance in other deposits [99–101].

Recent studies have shown that uranium oxyhydroxides are commonly the first alteration products resulting from weathering of the primary mineralisation [94,102,103]. However, both uranium oxyhydroxides and uranium silicates are rare in the Eureka deposit. A high activity of As and V anionic species in the solutions could potentially explain the scarcity of these minerals in the deposit. Alternatively, total replacement of these early oxyhydroxides by uranyl silicates, with subsequent replacement by uranyl phosphates, arsenates, sulphates and carbonates could have occurred if acidic ($pH < 7$) conditions were reached [93,94]. Moreover, given the wide mineralogical diversity observed within our samples, it is plausible that U^{6+} hydroxides and U^{6+} silicates are present in Eureka but were not sampled in our profiles. This would be consistent with the Shinkolobwe deposit in Congo, where uranium silicates formed only in the uppermost domains of a thick weathering profile [104].

Examples of late replacement processes similar to those described by [91,92] have been observed in the Eureka deposit, confirming that not all uranyl is fixed near the topographic surface. The occurrence of efflorescences of uranyl carbonates in the Eureka mine walls has been related to recent percolation of rainwater. Since sulphides inside the mines did not undergo extensive weathering, these percolating fluids would have a neutral pH. Previous works have shown that these conditions are ideal for the crystallization of some uranyl carbonates after uranyl carbonate complexes [92,105,106].

There is no evidence of weathering of the REE phosphates (i.e., monazite and xenotime), probably because once formed these phosphates are very resistant to weathering [107,108]. Finally, although molybdenite has not yet been found in the deposit, its occurrence can be inferred from the widespread abundance of wulfenite ($PbMoO_4$), a typical alteration product of molybdenite.

6.3. Conditions of Formation of the Stratabound Mineralisation

The detailed petrographic study of the stratabound mineralisation presented here has provided constraints on the temperature and pH of the main mineralisation of the Eureka mine. The mineral assemblage shows that it was formed at low temperature (200–400 °C) and slightly acidic conditions. However, there are several line of evidence that these conditions did not remain constant throughout the deposit formation. Additionally, the crystallization sequence defined from textural observations reveals that the formation of the stratabound mineralisation was often driven by out-of-equilibrium processes.

Low-temperature hydrothermal conditions of formation were first inferred from replacement of hematite by pyrite and bornite (Figure 6b,c), as well as the occurrence of chalcopyrite lamellae in bornite (Figure 7a). Experimental work by [109] demonstrated that replacement of hematite by pyrite and bornite from a Cu–H_2S-rich saline acidic fluid takes place at 200–300 °C. The extent of this replacement depends on changing pH conditions, driven by variable interaction of the percolating fluids with the cement, as well as on different fluid/rock ratios, which are controlled by the distance to the main tectonic structures. Moreover, fine chalcopyrite lamellae in bornite identical to those described in Eureka have also been reported in other red-bed examples [110] and many other deposits formed at low temperature conditions [111]. [110] carried out several experiments and proposed the existence of solid solutions up to 200 °C, lamellar exsolutions between 200 °C and 400 °C and a homogenization above this temperature. However, [109,112] pointed out that in natural systems a

hydrothermal fluid acts as catalyst for diffusion, based on experiments under hydrothermal conditions. These low temperatures are consistent with the low-grade metamorphism that has been reported in the Pre-Pyrenees [50]. These authors described the crystallization of prehnite-pumpellyite in the dolerites ("ophites") intruding Keuper facies in the Alpine nappes, at temperatures up to 250 °C.

The mineral assemblages of the Eureka deposit suggest that the main mineralisation was formed under acidic, although slightly variable, pH conditions. As mentioned above, replacement of the hematite cement by pyrite and bornite requires the infiltration of saline fluids with low pH [109]. These authors also stated that an acidic fluid prevents the development of pyrrhotite, which is also consistent with our observations in the Eureka mine. However, the occurrence of REE phosphates in Eureka (i.e., xenotime and monazite) in association with apatite (Figure 6f) is indicative of intermediate pH conditions, since aluminous phosphates would be more stable under more acidic conditions [113]. REE phosphates can also occur without apatite, which can be explained by local percolation of low-temperature hydrothermal fluids with lower pH. In these conditions, phosphates of the monazite group remain stable, while the higher solubility of apatite would not allow its formation [114]. The absence of Ce^{4+}-bearing minerals and the simultaneous precipitation of Ce with LREE in the monazite structure is also consistent with a local reducing environment.

The chalcopyrite-bornite-chalcopyrite sequence (Figure 7a) was also experimentally obtained by [112]. However, they explained these replacements as the result of out-of-equilibrium processes, which involve early replacement of chalcopyrite by bornite-digenite solid solutions at 300 °C, followed by a retrograde replacement of bornite by chalcopyrite at ~150 °C in acid pH conditions. Other evidence of out-of-equilibrium crystallization is identified from the replacement of pyrite by chalcopyrite, then by bornite and finally by chalcocite (Figure 7a), as a result of an increasing activity of copper in the hydrothermal fluids. Absence of equilibrium is easily explained by the movement of fluids along slaty cleavage and grain boundaries during Alpine deformation.

6.4. Eureka: A Metamorphite-Type Uranium Deposit?

Sandstone-type uranium deposits are commonly found in intermontane basins, over cratonic platforms, or in coastal embayment environments [115], and are directly linked to the hydrodynamics of subsiding basins [116]. However, the Eureka deposit clearly differs from a typical sandstone-type, as it has been interpreted to be syntectonic and associated with thrust stacking. In addition, the high temperatures proposed here for the Eureka deposit (between the 200 °C and 400 °C) are at odds with the diagenetic profile of the typical sandstone-type uranium deposit (below 200 °C).

Our results suggest that the ore-forming fluids in Eureka could have been related to low-grade metamorphic processes resulting from the thrust emplacement associated with the Alpine deformation. These features are characteristic of metamorphite-related uranium deposits [7]. In contrast with most of these deposits, extensive hydrothermal alteration (i.e., albitization, sericitisation, chloritisation, hematitisation, carbonatization, silicification [7]) has not been observed in Eureka. However, these alteration processes in metamorphite uranium deposits usually predate the main mineralizing event. Moreover, the lack of alteration in Eureka could be consistent with the silica-rich nature of the host rock and the relatively low temperatures (mostly 200–300 °C) inferred from the crystallization of the main mineralisation. In many metamorphite deposits there is an important structural control on the deposition of the ores. Although preferential transportation of the hydrothermal fluids through structural features cannot be ruled out in Eureka, it is more likely that ore deposition was related to the distribution of the organic matter in the sediments. This is consistent with previous works, where organic matter has also been interpreted to play a major role in the formation of deposits classified as metamorphite (e.g., Forstau in the Austrian Alps [117]). Therefore, with all necessary caution, we suggest that the Eureka deposit could be described as low-temperature, sandstone-hosted stratabound metamorphite U deposit.

7. Conclusions

The petrographic characterisation of the Eureka deposit revealed a unique mineralogical complexity and diversity encompassing characteristics previously observed in a variety of IAEA deposit types. Moreover, the Eureka deposit contains significant concentrations of critical elements in discrete minerals. In particular, REE minerals are widespread as fine-grained phases intergrown with roscoelite. Cobalt occurs as arsenides and sulpharsenides; bismuth, as sulphosalts and native bismuth; vanadium, mainly as roscoelite and secondary vanadates. Therefore, these elements could be a by-product of the beneficiation of Cu or U in this style of deposit, although the fine grain size of the ores can complicate their extraction.

The source of the HFSE could be the underlying Silurian black shales (the detachment level of many of the thrusts in the basement), whereas the source of U and REE is probably associated with the volcanic rocks of the area. The source of S is likely related to the nearby evaporitic sulphates of the Keuper facies, which are also the detachment level of many thrusts in the Pyrenees.

The deposit was formed during the Alpine orogeny, favored by hydrothermal fluid movement during thrusting. Most metals were transported as chloride complexes, and REE as sulphate complexes. The arrival of these hydrothermal fluids to the coal-bearing Triassic unit resulted in the reduction of the SO_4 in solution to S^{2-}, triggering the precipitation of the metals as sulphides, uraninite and roscoelite by interaction with the original cements. Reduction of the SO_4 complex to sulphide, combined with destabilization of fluorapatite, also forced the precipitation of REE as phosphates. The low temperature of the mineralizing fluids was most likely controlled by the prehnite-pumpellyite facies regional metamorphic conditions. The irregular distribution of mineral phases is here related to pH and chemical gradients in the deposit. These gradients are explained by the movement of the fluids along the slaty cleavage in rocks of different grain sizes and parageneses, resulting in diverse reactivity. Textural observations also suggest lack of equilibrium between the minerals and the fluids.

Supergene alteration resulted in the dispersion of some critical elements, such as nickel and cobalt, while vanadium was fixed as vanadates, and bismuth, as oxides. REE phosphates as monazite and xenotime are stable in this context.

Regardless of the origin of the fluids, the deposition of critical elements in Eureka was most likely controlled by the occurrence of organic matter. Therefore, other sandstone-hosted deposits in non-metamorphosed sedimentary basins could also be explored for the same critical elements found in Eureka if similar coal levels are present.

Supplementary Materials: The following are available online at http://www.mdpi.com/2075-163X/10/1/34/s1. Table S1: Major element composition of the minerals forming the primary and supergene mineralisations.

Author Contributions: Conceptualization, M.C.-O. and J.C.M.; methodology, M.C.-O., E.T. and J.C.M.; field work, M.C.-O., J.C.M., E.T., L.T., M.C., C.V.-d.-B.; investigation, M.C.-O., J.C.M., E.T., L.T., M.C., C.V.-d.-B., J.P.; writing—original draft preparation, J.C.M. and M.C.-O.; writing—review and editing, M.C.-O., J.C.M., E.T., L.T., M.C., C.V.-d-B., Y.D.-A., S.A.-C., J.X.; funding acquisition, J.C.M., J.P. All authors have read and agreed to the published version of the manuscript.

Funding: This study is part of the activities of the BCN SGA-SEG Student Chapter of the University of Barcelona, granted by the Society of Economic Geologists (SEG) and the Society of Geology Applied to Mineral Deposits (SGA), fitting in the activities of the Teaching Innovation Group MINREMIN GINDO-UB/172. Moreover, it is a contribution of the Consolidated Research Group AGAUR 20017 SGR707 de la Generalitat de Catalunya.

Acknowledgments: Xavier Llovet is acknowledged for their support in the microprobe analyses; Javier García Veigas, Eva Prats and David Artiaga gave support in the SEM-BSE-EDS analyses. The manuscript benefited of the corrections of three anonymous referees. This is contribution 1411 from the ARC Centre of Excellence for Core to Crust Fluid Systems (http://www.ccfs.mq.edu.au) and 1355 in the GEMOC Key Centre (http://www.gemoc.mq.edu.au).

Conflicts of Interest: The authors declare no conflict of interest.

References

1. Arribas, A. Mineralogía y metalogenia de los yacimientos españoles de uranio. Los indicios cuprouraníferos en el Trías de los Pirineos Catalanes. *Studia Geológica* **1966**, *222*, 31–45.
2. Abella, J.; Viñals, J. Cejkaïta, arsenuranilita, compreignacita, natrozippeïta i d'altres minerals rars d'urani en el jaciment "Mina Eureka". *Mineral. de Catalunya. Grup Mineralògic Català* **2009**, *10*, 52–71.
3. Ibáñez-Insa, J.; Elvira, J.J.; Llovet, X.; Pérez-Cano, J.; Oriols, N.; Busquets-Masó, M.; Hernández, S. Abellaite, $NaPb_2(CO_3)_2(OH)$, a new supergene mineral from the Eureka mine, Lleida province, Catalonia, Spain. *Eur. J. Mineral.* **2017**, *29*, 915–922. [CrossRef]
4. Finch, W.I.; Davis, J.F. Sandstone-type uranium deposits—An introduction. In *Geological Environments Sandstone-Type Uranium Deposits*; IAEA-TECDOC-328; IAEA: Viena, Austria, 1985; pp. 401–408.
5. Dahlkamp, F.J. *Uranium Ore Deposits*; Springer Science & Business Media: Berlin, Germany, 2013.
6. IAEA. *World Distribution of Uranium Deposits (UDEPO) with Uranium Deposit Classification*; TECDOC-1629; IAEA: Viena, Austria, 2009.
7. IAEA. *Geological Classification of Uranium Deposits and Description of Selected Examples*; IAEA-TECDOC-1842; IAEA: Viena, Austria, 2018.
8. Plant, J.A.; Simpson, P.R.; Smith, B.; Windley, B.F. Uranium ore deposits. Products of the reactive Earth. In *Uranium: Mineralogy, Geochemistry and the Environment*; Burns, P.C., Finch, R., Eds.; Washington, DC, USA, 1999; pp. 91–180.
9. Fischer, R.P. Uranium-bearing sandstone deposits of the Colorado Plateau. *Econ. Geol.* **1950**, *45*, 1–11. [CrossRef]
10. Wright, R.J. Ore controls in sandstone uranium deposits of the Colorado Plateau. *Econ. Geol.* **1955**, *50*, 135–155. [CrossRef]
11. Jensen, M.L. Sulfur isotopes and the origin of sandstone-type uranium deposits. *Econ. Geol.* **1958**, *53*, 598–616. [CrossRef]
12. Bruneton, P.; Cuney, M. Geology of uranium deposits. In *Uranium for Nuclear Power*; Woodhead Publishing: Sawston, UK, 2016; pp. 11–52.
13. Akhtar, S.; Yang, X.; Pirajno, F. Sandstone type uranium deposits in the Ordos Basin, Northwest China: A case study and an overview. *J. Asian Earth Sci.* **2017**, *146*, 367–382. [CrossRef]
14. Abzalov, M.Z. Sandstone-hosted uranium deposits amenable for exploitation by in situ leaching technologies. *Appl. Earth Sci.* **2012**, *121*, 55–64. [CrossRef]
15. Spirakis, C. The roles of organic matter in the formation of uranium deposits in sedimentary rocks. *Ore Geol. Rev.* **1996**, *11*, 53–69. [CrossRef]
16. Jaireth, S.; McKay, A.; Lambert, I. Association of large sandstone uranium deposits with hydrocarbons. *AusGeo News* **2008**, *89*, 6.
17. Burrows, D.R. Uranium exploration in the past 15 years and recent advances in uranium metallogenic models. In *The Challenge of Finding New Mineral Resources: Global Metallogeny, Innovative Exploration and New Discoveries*; Goldfarb, R.J., Marsh, E.E., Monecke, T., Eds.; SEG: Denver, CO, USA, 2010; Volume II: Zinc-Lead, Nickel-Copper-PGE and Uranium, pp. 599–652.
18. Goldhaber, M.B.; Reynolds, R.L.; Rye, R.O. Role of fluid mixing and fault-related sulfide in the origin of the Ray Point Uranium District, South Texas. *Econ. Geol.* **1983**, *78*, 1043–1062. [CrossRef]
19. Grandell, L.; Lehtilä, A.; Kivinen, M.; Koljonen, T.; Kihlman, S.; Lauri, L.S. Role of critical metals in the future markets of clean energy technologies. *Renew. Energy* **2016**, *95*, 53–62. [CrossRef]
20. Vidal-Legaz, B.; Mancini, L.; Blengini, G.A.; Pavel, C.; Marmier, A.; Blagoeva, D.; Latunussa, C.; Nuss, P.; Dewulf, J.; Nita, V.; et al. *Raw Materials Scoreboard*; Publications Office of the European Union: Bruxelles, Belgium, 2016.
21. Wall, F.; Rollat, A.; Pell, R.S. Responsible sourcing of critical metals. *Elements* **2017**, *13*, 313–318. [CrossRef]
22. Mathieux, F.; Ardente, F.; Bobba, S.; Nuss, P.; Blengini, G.A.; Alves Dias, P.; Blagoeva, D.; Torres de Matos, C.; Wittmer, D.; Pavel, C.; et al. *Critical Raw Materials and the Circular Economy*; Publications Office of the European Union: Bruxelles, Belgium, 2017.
23. Roberti, K.J. *Geological Map of the Flamisell and Mañanet Valleys (1:25.000 Scale)*; Geological Institute, Leiden University: Leiden, The Netherlands, 1970.

24. Sanz-López, J. Devonian and Carboniferous pre-Stephanian rocks from the Pyrenees. In *Palaeozoic Conodonts from Northern Spain*; García-López, S., Bastida, F., Eds.; Serie Cuadernos del Museo Geominero; Instituto Geológico y Minero de España: Madrid, Spain, 2002; pp. 1376–1389.
25. Aguilar, C.; Liesa, M.; Castiñeiras, P.; Navidad, M. Late Variscan metamorphic and magmatic evolution in the eastern Pyrenees revealed by U–Pb age zircon dating. *J. Geol. Soc.* **2014**, *171*, 181–192. [CrossRef]
26. de Hoÿm de Marien, L.; Le Bayon, B.; Pitra, P.; Van Den Driessche, J.; Poujol, M.; Cagnard, F. Two-stage Variscan metamorphism in the Canigou massif: Evidence for crustal thickening in the Pyrenees. *J. Metamorph. Geol.* **2019**, *37*, 863–888. [CrossRef]
27. Van Lichtervelde, M.; Grand'Homme, A.; de Saint-Blanquat, M.; Olivier, P.; Gerdes, A.; Paquette, J.-L.; Melgarejo Draper, J.C.; Druguet, E.; Alfonso Abella, M.P. U–Pb geochronology on zircon and columbite-group minerals of the Cap de Creus pegmatites, NE Spain. *Mineral. Petrol.* **2017**, *111*, 1–21. [CrossRef]
28. ICGC Mapa Geològic de Catalunya. Available online: http://betaportal.icgc.cat/visor/client_utfgrid_geo.html (accessed on 26 March 2019).
29. Mey, P.H.W.; Nagtegall, P.J.; Roberti, K.J.; Harteweelt, J.J.A. Ithostratigraphic subdivision of post-Hercynian deposits in the south-central Pyrenees. *Leidse Geol. Meded.* **1968**, *41*, 221–228.
30. Martí, J. La formación volcánica estefaniense de Erill Castell (Pirineo de Lérida). *Acta Geol. Hisp.* **1983**, *18*, 27–34.
31. Besly, B.; Collinson, J.D. Volcanic and tectonic controls of lacustrine and alluvial sedimentation in the Stephanian coal-bearing sequence of the Malpás-Sort Basin, Catalonian Pyrenees. *Sedimentology* **1991**, *38*, 3–26. [CrossRef]
32. Martí, J. Genesis of crystal-rich volcanicastic facies in the Permian red beds of the Central Pyreneees (NE Spain). *Sediment. Geol.* **1996**, *106*, 1–19. [CrossRef]
33. Soriano, C.; Martí, J.; Casas, J.M. Palinspatic reconstruction of Permo-Carboniferous basins involved in Alpine deformation: The Erill Castell-Estac basin, Southern pyrenees, Spain. *Geologie Mijnbouw* **1996**, *75*, 43–55.
34. Calvet, F.; Anglada, E.; Salvany, J.M. El Triásico de los Pirineos. In *Geología de España*; Vera, J.A., Ed.; SGE-IGME: Madrid, Spain, 2004; pp. 272–274.
35. López-Gómez, J.; Alonso-Azcárate, J.; Arche, A.; Arribas, J.; Fernández Barrenechea, J.; Borruel-Abadía, V.; Bourquin, S.; Cadenas, P.; Cuevas, J.; De la Horra, R.; et al. Permian-Triassic Rifting Stage. In *The Geology of Iberia: A Geodynamic Approach*; Quesada, C., Oliveira, J.T., Eds.; Springer International Publishing: Cham, Switzerland, 2019; Volume 3, pp. 29–112.
36. Mujal, E.; Gretter, N.; Ronchi, A.; López-Gómez, J.; Falconnet, J.; Díez, J.B.; De la Horra, R.; Bolet, A.; Oms, O.; Arche, A.; et al. Constraining the Permian/Triassic transition in continental environments: Stratigraphic and paleontological record from the Catalan Pyrenees (NE Iberian Peninsula). *Palaeogeogr. Palaeoclimatol. Palaeoecol.* **2016**, *445*, 18–37. [CrossRef]
37. Lloret, J.; Ronchi, A.; López-Gómez, J.; Gretter, N.; De la Horra, R.; Barrenechea, J.F.; Arche, A. Syn-tectonic sedimentary evolution of the continental late Palaeozoic-early Mesozoic Erill Castell-Estac Basin and its significance in the development of the central Pyrenees Basin. *Sediment. Geol.* **2018**, *374*, 134–157. [CrossRef]
38. Gretter, N.; Ronchi, A.; López-Gómez, J.; Arche, A.; De la Horra, R.; Barrenechea, J.; Lago, M. The Late Palaeozoic-Early Mesozoic from the Catalan Pyrenees (Spain): 60Myr of environmental evolution in the frame of the western peri-Tethyan palaeogeography. *Earth-Sci. Rev.* **2015**, *150*, 679–708. [CrossRef]
39. Calvet, F.; Sole de Porta, N.; Salvany, J.M. Cronoestratigrafía (palinología) del Triásico sudpirenaico y del Pirineo Vasco-Cantábrico. *Acta Geol. Hisp.* **1993**, *28*, 33–48.
40. Salvany, J.M.; Bastida, J. Análisis litoestratigráfico del Keuper surpirenaico central. *Revista Sociedad Geológica España* **2004**, *17*, 3–26.
41. Rossi, P.; Cocherie, A.; Fanning, C.M.; Ternet, Y. Datation UPb sur zircons des dolérites tholéiitiques pyrénéennes (ophites) à la limite Trias-Jurassique et relations avec les tufs volcaniques dits «infra-liasiques» nord-pyrénéens. *C. R. Géosci.* **2003**, *335*, 1071–1080. [CrossRef]
42. Durand-Wackenheim, C.; Thiebaut, J. Contribution a l'etude des processus de scapolitisation des ophites des Pyrenees. *Bull. Soc. Géol. France* **1986**, *2*, 629–635. [CrossRef]
43. Mencos, J.; Carrera, N.; Munoz, J.A. Influence of rift basin geometry on the subsequent postrift sedimentation and basin inversion: The Organyà Basin and the Bóixols thrust sheet (south central Pyrenees). *Tectonics* **2015**, *34*, 1452–1474. [CrossRef]

44. Vergés, J.; García-Senz, J. Mesozoic evolution and Cainozoic inversion of the Pyrenean Rift. In *Peri-Tethys Memoir 6: Peri-Tethyan Rift/Wrench Basins and Passive Margins*; Ziegler, P.A., Cavazza, W., Robertson, A.H.F., Crasquin-Soleau, S., Eds.; French National Museum Natural History: Paris, France, 2001; pp. 187–212.
45. Teixell, A. The Ansó transect of the southern Pyrenees: Basement and cover thrust geometries. *J. Geol. Soc.* **1996**, *153*, 301–310. [CrossRef]
46. Vergés, J.; Muñoz, J.A. Thrust sequences in the southern central Pyrenees. *Bull. Soc. Géol. France* **1990**, *8*, 265–271. [CrossRef]
47. Mellere, D. Thrust-generated, back-fill stacking of alluvial fan sequences, south-central Pyrenees, Spain (La Pobla de Segur Conglomerates). In *Tectonic Controls and Signatures in Sedimentary Successions*; Frostick, L.E., Steel, R.J., Eds.; Blackwell Science: Oxford, UK, 1993; pp. 259–276.
48. Sinclair, H.D.; Gibson, M.; Naylor, M.; Morris, R.G. Asymmetric growth of the Pyrenees revealed through measurement and modeling of orogenic fluxes. *Am. J. Sci.* **2005**, *305*, 369–406. [CrossRef]
49. Saura, S.; Teixell, A. Inversion of small basins: Effects on structural variations at the leading edge of the Axial Zone antiformal stack (Southern Pyrenees, Spain). *J. Struct. Geol.* **2006**, *28*, 1909–1920. [CrossRef]
50. Crespi, A.; Rius, J.; Melgarejo, J.C. Nuevos datos sobre el contexto geológico de la aerinita en el dominio pirenaico. *Macla* **2009**, *11*, 63–64.
51. Ramsay, J.G. *Plegamiento y Fracturación de Rocas*; H Blume: Madrid, Spain, 1977; pp. 410–415.
52. Siivola, J.; Schmid, R. Recommendations by the IUGS Subcommission on the Systematics of Metamorphic Rocks: List of Mineral Abbreviations. Available online: https://www.bgs.ac.uk/scmr/docs/papers/paper_12.pdf (accessed on 1 February 2007).
53. Kompanchenko, A.A.; Voloshin, A.V.; Balagansky, V. Vanadium mineralisation in the Kola region, Fennoscandian shield. *Minerals* **2018**, *8*, 474. [CrossRef]
54. Ibáñez-Insa, J.; Elvira, J.J.; Oriols, N.; Llovet, X.; Viñals, J. Abellaite, IMA 2014-111. *Mineral. Mag.* **2016**, *80*, 199–205.
55. Rose, A.W.; Wright, R.J. Geochemical exploration models for sedimentary uranium deposits. *J. Geochem. Explor.* **1980**, *13*, 153–179. [CrossRef]
56. Cai, C.; Li, H.; Qin, M.; Luo, X.; Wang, F.; Ou, G. Biogenic and petroleum-related ore-forming processes in Dongsheng uranium deposit, NW China. *Ore Geol. Rev.* **2007**, *32*, 262–274. [CrossRef]
57. Cai, C.; Dong, H.; Li, H.; Xiao, X.; Ou, G.; Zhang, C. Mineralogical and geochemical evidence for coupled bacterial uranium mineralisation and hydrocarbon oxidation in the Shashagetai deposit, NW China. *Chem. Geol.* **2007**, *236*, 167–179. [CrossRef]
58. Bonnetti, C.; Liu, X.; Zhaobin, Y.; Cuney, M.; Michels, R.; Malartre, F.; Mercadier, J.; Cai, J. Coupled uranium mineralisation and bacterial sulphate reduction for the genesis of the Baxingtu sandstone-hosted U deposit, SW Songliao Basin, NE China. *Ore Geol. Rev.* **2017**, *82*, 108–129. [CrossRef]
59. Yang, X.; Ling, M.; Sun, W.; Luo, X.; Lai, X.; Liu, C.; Miao, J.; Sun, W. The genesis of sandstone-type uranium deposits in the Ordos Basin, NW China: Constraints provided by fluid inclusions and stable isotopes. *Int. Geol. Rev.* **2009**, *51*, 422–455. [CrossRef]
60. Breit, G.N.; Goldhaber, G.N.; Shawe, D.R.; Simmons, E.C. Authigenic barite as an indicator of fluid movement through sandstones within the colorado plateau. *J. Sediment. Res.* **1990**, *60*, 884–896.
61. Nash, J.T. Uranium deposits in the Jackpile sandstone, New Mexico. *Econ. Geol.* **1968**, *63*, 737–750. [CrossRef]
62. Angiboust, S.; Fayek, M.; Power, I.M.; Camacho, A.; Calas, G.; Southam, G. Structural and biological control of the Cenozoic epithermal uranium concentrations from the Sierra Peña Blanca, Mexico. *Miner. Depos.* **2012**, *47*, 859–874. [CrossRef]
63. Bonnetti, C.; Cuney, M.; Malartre, F.; Michels, R.; Liu, X.; Peng, Y. The Nuheting deposit, Erlian Basin, NE China: Synsedimentary to diagenetic uranium mineralisation. *Ore Geol. Rev.* **2015**, *69*, 118–139. [CrossRef]
64. Bonnetti, C.; Cuney, M.; Michels, R.; Truche, L.; Malartre, F.; Liu, X.; Yang, J. The multiple roles of sulfate-reducing bacteria and Fe–Ti oxides in the genesis of the bayinwula roll front-type uranium deposit, Erlian Basin, NE China. *Econ. Geol.* **2015**, *110*, 1059–1081. [CrossRef]
65. Bonnetti, C.; Cuney, M.; Bourlange, S.; Deloule, E.; Poujol, M.; Liu, X.; Peng, Y.; Yang, J. Primary uranium sources for sedimentary-hosted uranium deposits in NE China: Insight from basement igneous rocks of the Erlian Basin. *Miner. Depos.* **2017**, *52*, 297–315. [CrossRef]
66. Shawe, D. *Uranium-Vanadium Deposits of the Slick Rock District, Colorado*; U.S. Geological Survey Professional Paper 576-F; U.S. Geological Survey: Reston, VA, USA, 2011; p. 80.

67. García-Sansegundo, J.; Poblet, J.; Alonso, J.L.; Clariana, P. Hinterland-foreland zonation of the Variscan orogen in the Central Pyrenees: Comparison with the northern part of the Iberian Variscan Massif. *Geol. Soc. Lond. Spec. Publ.* **2011**, *349*, 169–184. [CrossRef]
68. Canet, C.; Alfonso, P.; Melgarejo, J.C.; Jorge, S. V-rich minerals in contact-metamorhosed Silurian sedex deposits in the Poblet area, southwestern Catalonia, Spain. *Can. Mineral.* **2003**, *41*, 561–580. [CrossRef]
69. Canet, C.; Alfonso, P.; Melgarejo, J.; Jorge, S. PGE-bearing minerals in Silurian sedex deposits in the Poblet area, southwestern Catalonia, Spain. *Can. Mineral.* **2003**, *41*, 581–595. [CrossRef]
70. Tribovillard, N.; Algeo, T.J.; Lyons, T.; Riboulleau, A. Trace metals as paleoredox and paleoproductivity proxies: An update. *Chem. Geol.* **2006**, *232*, 12–32. [CrossRef]
71. Vine, J.D.; Tourtelot, E. Geochemistry of black shale deposits-A summary report. *Econ. Geol.* **1970**, *65*, 253–272. [CrossRef]
72. Algeo, T.J.; Maynard, J.B. Trace-metal covariation as a guide to water-mass conditions in ancient anoxic marine environments. *Geosphere* **2008**, *4*, 872. [CrossRef]
73. Hodgson, G.W. Vanadium, nickel and iron trace metals in crude oils of western Ganada. *AAPG Bull.* **1954**, *38*, 2537–2554.
74. Mast, R.F.; Ruch, R.R.; Meents, W.F. *Vanadium in Devonian, Silurian, and Ordovician Crude Oils of Lllinois*; Illinois State Geological Survey Circular: Champaign, IL, USA, 1973.
75. Höller, W.; Stumpfl, E.F. Cr–V oxides from the Rampura Agucha Pb–Zn–(Ag) deposit, Rajasthan, India. *Can. Mineral.* **1995**, *33*, 745–752.
76. Pan, Y.; Fleet, M.E. Mineral chemistry and geochemistry of vanadian silicates in the Hemlo gold deposit, Ontario, Canada. *Contrib. Mineral. Petrol.* **1992**, *109*, 511–525. [CrossRef]
77. Garrels, R.M.; Pommer, A.M. Part 14: Some quantitative aspects of the oxidation and reduction of the ores. *Geol. Surv. Bull.* **1959**, *320*, 157–164.
78. Seward, T.M.; Williams-Jones, A.E.; Migdisov, A.A. The chemistry of metal transport and deposition by ore-forming hydrothermal fluids. In *Treatise on Geochemistry*; Elsevier: Amsterdam, The Netherlands, 2014; pp. 29–57.
79. Canals, A.; Cardellach, E.; Rey, D.M.; Ayora, C. Origin of the Atrevida vein (Catalonian Coastal Ranges, Spain): Mineralogic, fluid inclusion and stable isotope study. *Econ. Geol.* **1992**, *87*, 142–153. [CrossRef]
80. Skirrow, R.G.; Jaireth, S.; Huston, D.L.; Bastrakov, E.N.; Schofield, A.; van der Wielen, S.E.; Barnicoat, A.C. *Uranium Mineral Systems: Processes, Exploration Criteria and A New Deposit Framework*; Geoscience Australia: Canberra, Australia, 2009.
81. Díaz-acha, Y.; Campeny, M.; Tauler, E.; Bosch, J.; Melgarejo, J.C.; Díaz-ontiveros, I.; Fernández-lluch, D.; Proenza, J.A.; Andreazini, A. Critical elements in supergene phosphates: The example of the weathering profile at the Gavà Neolithic mines, Catalonia, Spain. *Minerals* **2020**, *10*, 3. [CrossRef]
82. Ito, J. Synthesis of vanadium silicates: Haradaite, goldmanite and roscoelite. *Miner. J.* **1965**, *4*, 299–316. [CrossRef]
83. Migdisov, A.A.; Reukov, V.V.; Williams-Jones, A.E. A spectrophotometric study of neodymium (III) complexation in sulfate solutions at elevated temperatures. *Geochim. Cosmochim. Acta* **2006**, *70*, 983–992. [CrossRef]
84. Migdisov, A.A.; Williams-Jones, A.E. A spectrophotometric study of Nd(III), Sm(III) and Er(III) complexation in sulfate-bearing solutions at elevated temperatures. *Geochim. Cosmochim. Acta* **2008**, *72*, 5291–5303. [CrossRef]
85. Ward, C.R.; Corcoran, J.F.; Saxby, J.D.; Read, H.W. Occurrence of phosphorus minerals in Australian coal seams. *Int. J. Coal Geol.* **1996**, *30*, 185–210. [CrossRef]
86. Pirard, C.; Hatert, F. The sulfides and selenides of the Musonoi mine, Kolwezi, Katanga, Democratic Republic of Congo. *Can. Mineral.* **2008**, *46*, 219–231. [CrossRef]
87. Timofeev, A.; Migdisov, A.A.; Williams-Jones, A.E.; Roback, R.; Nelson, A.T.; Xu, H. Uranium transport in acidic brines under reducing conditions. *Nat. Commun.* **2018**, *9*, 1469. [CrossRef] [PubMed]
88. Liu, C.; Eleish, A.; Hystad, G.; Golden, J.J.; Downs, R.T.; Morrison, S.M.; Hummer, D.R.; Ralph, J.P.; Fox, P.; Hazen, R.M. Analysis and visualization of vanadium mineral diversity and distribution. *Am. Mineral.* **2018**, *103*, 1080–1086. [CrossRef]
89. Evans, H.T.J.; Garrels, R.M. Thermodynamic equilibria of vanadium in aqueous systems as applied to the interpretation of the Colorado Plateau ore deposits. *Geochim. Cosmochim. Acta* **1958**, *15*, 131–149. [CrossRef]

90. Weeks, A.D. Mineralogy and geochemistry of vanadium in the Colorado Plateau. *J. Less Common Met.* **1961**, *3*, 443–450. [CrossRef]
91. Ondruš, P.; Veselovský, F.; Gabašová, A.; Drábek, M.; Dobes, P.; Maly, K.; Hloušek, J.; Sejkora, J. Ore-forming processes and mineral parageneses of the Jáchymov ore district. *J. Geosci.* **2003**, *48*, 157–192.
92. Finch, R.; Murakami, T. Systematics and paragenesis of uranium minerals. In *Uranium: Mineralogy, Geochemistry and the Environment*; Burns, P.C., Finch, R., Eds.; de Gruyter: Berlin, Germany, 1999; pp. 91–180.
93. Krivovichev, S.V.; Plášil, J. Mineralogy and crystallography of uranium. In *Uranium: From Cradle to Grave*; Burns, P.C., Sigmon, G.E., Eds.; Mineralogical Association of Canada Short Courses: Quebec City, QC, Canada, 2013; Volume 43, pp. 15–119.
94. Plášil, J. Oxidation-hydration weathering of uraninite: The current state-of-knowledge. *J. Geosci.* **2014**, *59*, 99–114. [CrossRef]
95. Evans, H.T. Part 7: The cristal chemistry and mineralogy of vanadium. *Geol. Surv. Bull.* **1959**, *320*, 91–102.
96. Tokunaga, T.K.; Kim, Y.; Wan, J.; Yang, L. Aqueous uranium(VI) concentrations controlled by calcium uranyl vanadate precipitates. *Environ. Sci. Technol.* **2012**, *46*, 7471–7477. [CrossRef] [PubMed]
97. Spano, T.L.; Dzik, E.A.; Sharifironizi, M.; Dustin, M.K.; Turner, M.; Burns, P.C. Thermodynamic investigation of uranyl vanadate minerals: Implications for structural stability. *Am. Mineral.* **2017**, *102*, 1149–1153. [CrossRef]
98. De Putter, T.; Mees, F.; Decrée, S.; Dewaele, S. Supergene copper deposits and minerals in the world-class SHSC deposits of the Central African Copperbelt (Katanga, DRC). In Proceedings of the Let's Talk Ore Deposits, Antofagasta, Chile, 26–29 September 2011; Barra, F., Reich, M., Campos, E., Tornos, F., Eds.; Ediciones Univ Catolica del Norte: Antofagasta, Chile, 2011; pp. 838–840.
99. Kanzari, A.; Gérard, M.; Boekhout, F.; Galoisy, L.; Calas, G.; Descostes, M. Impact of incipient weathering on uranium migration in granitic waste rock piles from former U mines (Limousin, France). *J. Geochem. Explor.* **2017**, *183*, 114–126. [CrossRef]
100. Jensen, K.A.; Palenik, C.S.; Ewing, R.C. U^{6+} phases in the weathering zone of the Bangombe U-deposit: Observed and predicted mineralogy. *Radiochim. Acta* **2002**, *90*, 1–9. [CrossRef]
101. Jerden, J.; Sinha, A.; Zelazny, L. Natural immobilization of uranium by phosphate mineralisation in an oxidizing saprolite–soil profile: Chemical weathering of the Coles Hill uranium deposit, Virginia. *Chem. Geol.* **2003**, *199*, 129–157. [CrossRef]
102. Finch, R.J.; Ewing, R.C. The corrosion of uraninite under oxidizing conditions. *J. Nucl. Mater.* **1992**, *190*, 133–156. [CrossRef]
103. Brugger, J.; Meisser, N.; Etschmannnn, B.; Ansermet, S.; Pring, A. Paulscherrerite from the Number 2 Workings, Mount Painter Inlier, Northern Flinders Ranges, South Australia: "Dehydrated schoepite" is a mineral after all. *Am. Mineral.* **2011**, *96*, 229–240. [CrossRef]
104. Deliens, M. Associations de minéraux sécondaires d'uranium à Shinkolobwe (région du Shaba, Zaïre). *Bulletin Minéralogie* **1977**, *100*, 32–38. [CrossRef]
105. Bullwinkel, E.P. *The Chemistry of Uranium in Carbonate Solutions*; Merrill Company: Saint Paul, MN, USA, 1954; p. RMO-2614.
106. Krestou, A.; Panias, D. Uranium (VI) speciation diagrams in the $UO_2^{2+}/CO_3^{2-}/H_2O$ system at 25 °C. *Eur. J. Miner. Process. Environ. Prot.* **2004**, *4*, 113–129.
107. Mariano, A.N. Economic geology of rare earth minerals. In *Geochemistry and Mineralogy of Rare Earth Elements. Mineralogical Society of America Reviews in Mineralogy 21*; Lipin, B.R., McCay, G., Eds.; Mineralogical Society of America: Chelsea, MI, USA, 1989; pp. 309–338.
108. McLennan, S.N. Rare earth elements in sedimentary rocks: Influence of provenance and sedimentary processes. In *Geochemistry and Mineralogy of Rare Earth Elements. Mineralogical Society of America Reviews in Mineralogy 21*; Lipin, B.R., McCay, G.A., Eds.; Mineralogical Society of America: Chelsea, MI, USA, 1989; pp. 169–200.
109. Zhao, J.; Brugger, J.; Chen, G.; Ngothai, Y.; Pring, A. Experimental study of the formation of chalcopyrite and bornite via the sulfidation of hematite: Mineral replacements with a large volume increase. *Am. Mineral.* **2014**, *99*, 343–354. [CrossRef]
110. Gaucher, E. A possible solution of the paradox of sedimentary bornite. *Econ. Geol.* **1963**, *59*, 303–308. [CrossRef]

111. Hatert, F. Transformation sequences of copper sulphides at Vielsalm, Stavelot Massif, Belgium. *Can. Mineral.* **2005**, *43*, 623–635. [CrossRef]
112. Li, K.; Brugger, J.; Pring, A. Exsolution of chalcopyrite from bornite-digenite solid solution: An example of a fluid-driven back-replacement reaction. *Miner. Depos.* **2018**, *53*, 903–908. [CrossRef]
113. Vieillard, P.; Tardy, Y.; Nahon, D. Stability fields of clays and aluminum phosphates: Parageneses in lateritic weathering of argillaceous phosphatic sediments. *Am. Mineral.* **1979**, *64*, 626–634.
114. Gysi, A.P.; Harlov, D.; Miron, G.D. The solubility of monazite ($CePO_4$), $SmPO_4$, and $GdPO_4$ in aqueous solutions from 100 to 250 °C. *Geochim. Cosmochim. Acta* **2018**, *242*, 143–164. [CrossRef]
115. Everhart, D.L. *Tectonic Settings of the World's Sandstone-Type Uranium Deposits*; International Atomic Energy Agency: Vienna, Austria, 1985.
116. Jin, R.; Teng, X.; Li, X.; Si, Q.; Wang, W. Genesis of sandstone-type uranium deposits along the northern margin of the Ordos Basin, China. *Geosci. Front.* **2020**, *11*, 215–277. [CrossRef]
117. Dahlkamp, F.J.; Scivetti, N. *Austria. International Uranium Resources Evaluation Project*; OECD: Paris, France, 1981.